

For Reference

NOT TO BE TAKEN FROM THIS ROOM

Ex libris
UNIVERSITATIS
ALBERTAENSIS





Digitized by the Internet Archive
in 2020 with funding from
University of Alberta Libraries

<https://archive.org/details/Hutton1971>

THE UNIVERSITY OF ALBERTA

STRESS ANALYSIS OF A BELLOWS EXPANSION JOINT

BY



J. STUART HUTTON

A THESIS

SUBMITTED TO THE FACULTY OF GRADUATE STUDIES AND RESEARCH
IN PARTIAL FULFILLMENT OF THE REQUIREMENTS FOR THE
DEGREE OF MASTER OF SCIENCE

DEPARTMENT OF MECHANICAL ENGINEERING

EDMONTON, ALBERTA

FALL, 1971

Thesis
1971
116

UNIVERSITY OF ALBERTA
FACULTY OF GRADUATE STUDIES AND RESEARCH

The undersigned certify that they have read, and recommend to the Faculty of Graduate Studies and Research for acceptance, a thesis entitled "Stress Analysis of a Bellows Expansion Joint" submitted by J. Stuart Hutton in partial fulfillment of the requirements for the degree of Master of Science.

Date *Oct. 19, 1971*

ABSTRACT

A theoretical analysis is presented for the problem of an axially loaded expansion joint or bellow consisting of a shell of revolution, with deep periodic corrugations. The problem is described analytically by two simultaneous differential equations. The solutions are given in terms of functions which are evaluated by numerical integration and tabulated.

Experimental results are presented for the case of axial loading which agree reasonably with the theoretical work.

ACKNOWLEDGMENTS

The author would like to thank Dr. J.R. Colbourne for his supervision of this thesis, Mr. F. Christopher for his aid in the experimental preparation and Miss H. Wozniuk for typing of this thesis.

The author is also grateful for funds made available from the National Research Council under Grant No. A-5163.

TABLE OF CONTENTS

	<u>Page</u>
Abstract	iii
Acknowledgments	iv
Table of Contents	v
List of Illustrations	vi
Nomenclature	vii
Introduction	1
Chapter I Derivation of the Equations	3
Chapter II Solution of Equations	20
2.1 Outer Solution	
2.2 Inner Solution	
Chapter III Experimental Investigation	38
Chapter IV Discussion of Results	47
Chapter V Concluding Remarks	54
References	56
Appendix A Determination of Experimental Parameters	57
Appendix B Experimental Data	59
Appendix C Values of $f(\rho)$ and $g(\rho)$	65

LIST OF ILLUSTRATIONS

<u>Figure</u>		<u>Page</u>
1.1	Undeformed and deformed shell element	5
1.2	Equilibrium of shell element	9
1.3	Cross-sectional profile	16
1.4	Assumed shape compared to a circular arc	17
2.1	Dependent variable $F(\xi)$	24
2.2	Dependent variable $G(\xi)$	25
2.3	Radial stresses	27
2.4	Circumferential stresses	28
2.5	Dependent variable $f(\rho)$	32
2.6	Dependent variable $g(\rho)$	33
2.7	Radial stresses	35
2.8	Circumferential stresses	36
3.1	Expansion joint	39
3.2	Strain gauges	39
3.3	S-shape profile	40
3.4	Location of strain gauges	42
3.5	Test set-up	43
4.1	Inner and outer solutions (radial)	48
4.2	Inner and outer solution (circumferential)	49
4.3	Radial stresses on inside surface	51
4.4	Circumferential stresses on inside surface	52

NOMENCLATURE

		First Appears <u>Page</u>
a b c \overline{c}	lengths defining the shell geometry	15
C	stiffness factor	12
D	stiffness factor	12
E	Young's modulus	11
f	function associated with a rotation	29
F	function associated with a rotation	20
F_0	parameter associated with a rotation	29
g	function associated with a stress	29
G	function associated with a stress	20
G_0	parameter associated with a stress	29
h	shell thickness	8
H	horizontal stress resultant	10
M	stress couple	10
N	stress resultant	8
p	pressure	10
P	total axial load	15
Q	shear stress resultant	8
r, r_0	radial coordinate	3
R_θ, R_ξ	principal radii of curvature	4

		First Appears Page
u	radial displacement	4
V	axial stress resultant	10
w	axial displacement	4
z, z_0	axial coordinate	3
α, α_0	length parameter for shell element	3
β	rotation	4
β_0	parameter associated with a rotation	21
ζ	shell thickness coordinate	9
η	dimensionless ratio \bar{c}/b	18
θ	polar angle	3
$\kappa_\xi, \kappa_\theta$	curvatures	6
λ	dimensionless ratio b/a	18
μ	dimensionless shell parameter	21
ν	Poisson's ratio	11
ξ	independent variable	3
ρ	independent variable	29
σ	stress	8
τ	inner solution magnification parameter	29
ϕ, ϕ_0	meridional angle	3
ψ_0	parameter associated with a stress	20

INTRODUCTION

The use in piping systems of expansion joints, or bellows, consisting of thin elastic shells of revolution is of importance to the design engineer. With a relatively easy method of determining the stresses and displacements, he is able to design economically for safety as well as for performance.

A paper by Clark [2], in 1950, presented methods of asymptotic integration for the analysis of thin elastic shells of revolution loaded symmetrically with respect to their axis. Expansion joints subject to axial loads and corrugated pipes subject to axial or internal pressure are used as examples of the general procedure developed by Clark.

In 1962, Laupa and Weil [6] presented an elastic analysis of U-shaped expansion joints under axial loads and internal or external pressure. Using the energy method for the toroidal section and combining the theory of flat plates, they were able to investigate any U-shaped bellows under any arbitrary combination of axial and pressure loading.

More recently, Clark [3] has solved the expansion problem again by asymptotic integration, but has put more emphasis on the analysis of the errors involved in the approximations. The cross-sectional profile he considered has the distinct advantage in that

it produces a smooth surface with continuous derivatives such that both principal curvatures are zero at a point of inflection of a meridian.

The analysis presented here follows the method used earlier by Reissner [1] to solve the toroidal shell of circular cross-section. The cross-sectional profile derived by Clark [3] is introduced into the governing differential equations and a solution has been found through numerical integration that can be compared with the numerical example presented by Clark [3] and with the experimental results carried out by the author.

In the solution of the differential equations, the terms inner and outer solutions are used. The former refers to that region of the solution where the boundary layer analysis exists; that is, there are relatively rapid changes in the dependent variables. The outer solution refers to that portion of the solution which does not exhibit a boundary layer phenomenon. In this region the bending stresses as well as the stresses due to rotation of the shell meridian are small compared with the primary membrane stresses.

CHAPTER I

DERIVATION OF THE EQUATIONS

The derivation of the governing equations for thin elastic shells of revolution follows that of Reissner [5]. The same notation that he used has been adopted here and is used throughout the thesis.

Geometrical Relations

The undeformed middle surface of a shell of revolution can be described in the form;

$$r = r(\xi) \quad z = z(\xi)$$

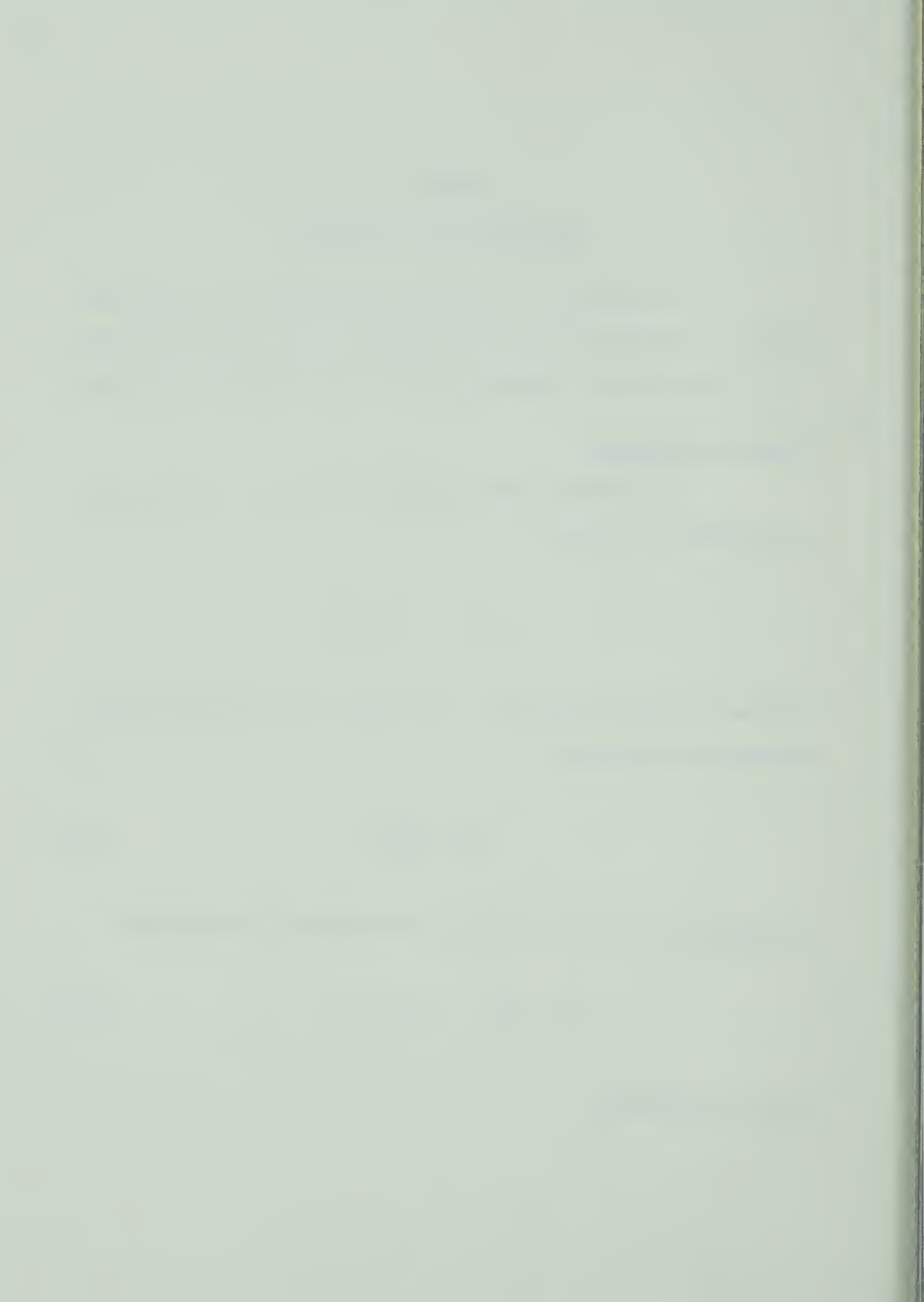
together with the polar angle θ . The angle of the tangents to the meridian (ϕ) is given by

$$\tan \phi = \frac{dz}{dr} \quad (1.1)$$

From equation (1.1), the following relationships can be derived:

$$\cos \phi = \frac{r'}{\alpha} \quad \sin \phi = \frac{z'}{\alpha} \quad (1.2)$$

where α is given by



$$\alpha = \{(r')^2 + (z')^2\}^{1/2}$$

and the primes denote differentiation with respect to ξ .

The principal radii of curvature of the middle surface of the undeformed surface of a shell of revolution are given by

$$\frac{1}{R_{\xi}} = \frac{\phi'}{\alpha} \quad (1.3)$$

$$\frac{1}{R_{\theta}} = \frac{\sin \phi}{r} \quad (1.4)$$

Analysis of Strain

Denoting the undeformed middle surface of the shell by the subscript 0, the deformed middle surface can be written in the form

$$r = r_0 + u \quad z = z_0 + w \quad (1.5)$$

where u and w are the displacements in the radial and axial directions respectively. The angle ϕ of the deformed surface can be written

$$\phi = \phi_0 - \beta$$

where β is a rotation between the deformed and undeformed meridians.

The assumption is made here that the deformations due to transverse shear strain are negligible as compared to one, and the

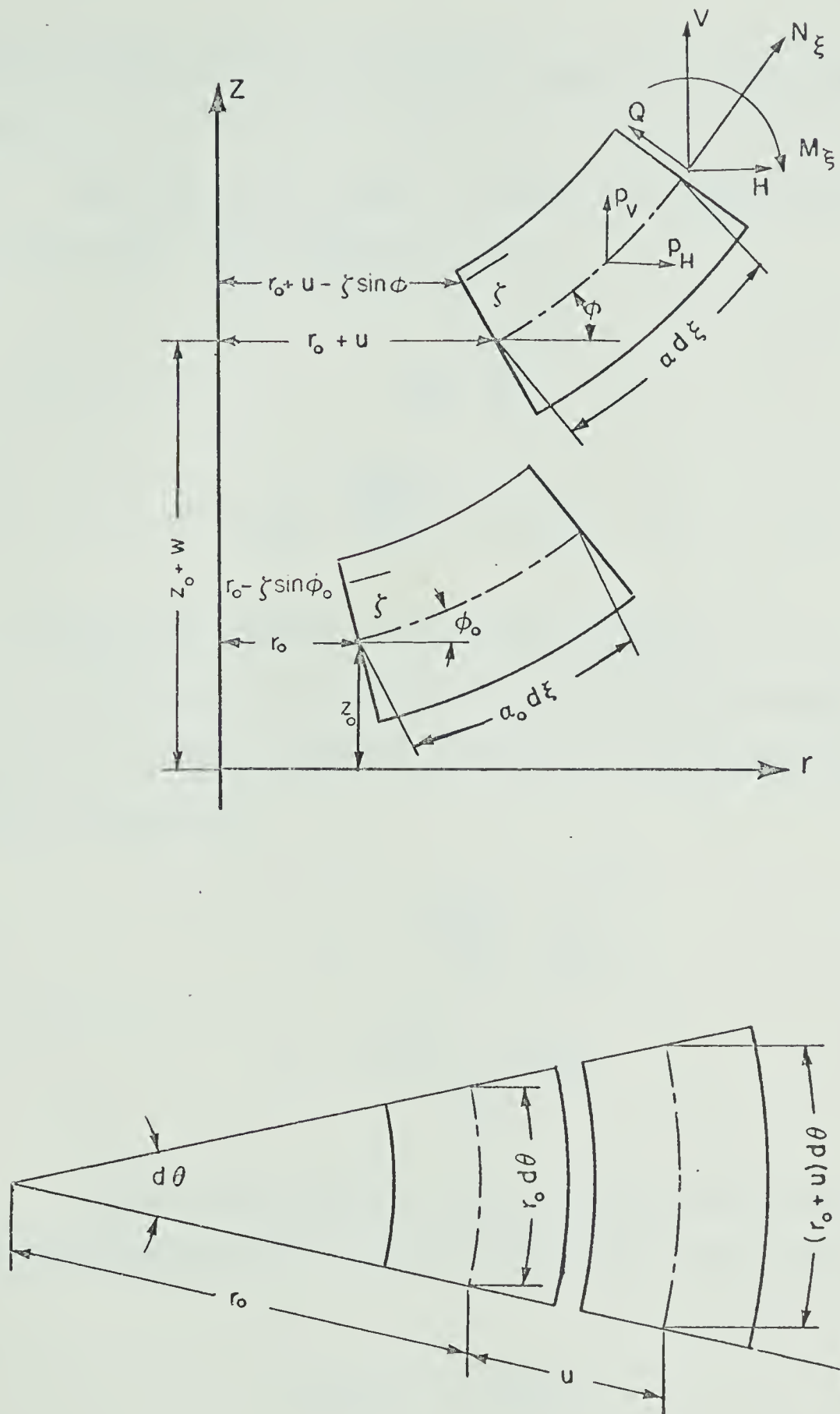


FIGURE 1.1 UNDEFORMED & DEFORMED SHELL ELEMENT



transverse normal stress is negligible compared with the remaining stresses.

With the aid of figure 1.1 the strains along the centre line of the shell can be shown to be

$$\epsilon_{\theta M} = \frac{u}{r_0} \quad (1.6)$$

$$\epsilon_{\xi M} = \frac{\cos \phi_0}{\cos \phi} \left\{ 1 + \frac{u'}{r_0} \right\} - 1 \quad (1.7)$$

where the subscript M refers to the middle surface.

Equations (1.3) and (1.4) can be written for both the deformed and the undeformed shell, and then the curvature differences κ_ξ and κ_θ are given by

$$\begin{aligned} \kappa_\xi &= - \left(\frac{\phi' - \phi_0'}{\alpha_0} \right) = \frac{\beta'}{\alpha_0} \\ \kappa_\theta &= - \left(\frac{\sin \phi - \sin \phi_0}{r_0} \right) \end{aligned} \quad (1.8)$$

The axial displacement w can be found by substituting equation (1.5) into equation (1.2). This gives the axial displacement as

$$(z_0 + w)' = \alpha \sin \phi \quad (1.9)$$

$$w' = \alpha \sin \phi - z_0'$$



The compatibility equation is derived by substituting the radial displacement u from equation (1.6) into equation (1.7).

$$\epsilon_{\xi M} = \frac{\cos\phi_0}{\cos\phi} \left(1 + \frac{(\epsilon_{\theta M} r_0)'}{r_0'} \right) - 1$$

which reduces to

$$\cos\phi_0 (r_0' \epsilon_{\theta M})' - \cos\phi (r_0' \epsilon_{\xi M}) = r_0' (\cos\phi - \cos\phi_0) \quad (1.10)$$

Equations (1.7), (1.8), (1.9) and (1.10) can be simplified by expanding in powers of β , and neglecting all terms except the first. The radial strain now becomes

$$\epsilon_{\xi M} = \frac{u'}{r_0} - \beta \tan\phi_0 - \frac{\beta u' \tan\phi_0}{r_0} \quad (1.11)$$

the circumferential curvature becomes

$$\kappa_{\theta} = \frac{\beta \cos\phi_0}{r_0} \quad (1.12)$$

the axial displacement becomes

$$w' = z_0' \epsilon_{\xi M} - (1 + \epsilon_{\xi M}) \beta r_0' \quad (1.13)$$

and finally the compatibility equation becomes

$$\cos\phi_0(r_0'\epsilon_{\theta M})' - (\cos\phi_0 + \beta\sin\phi_0)(r_0'\epsilon_{\xi M}) = r_0'(\beta\sin\phi_0) \quad (1.14)$$

Stress Resultants and Couples

Since the shell is axially symmetric and only axially symmetric loads are being considered, there will be no dependence upon the polar angle θ . Because of the independence upon θ , there will be only four stress components σ_ξ , σ_θ , σ_ζ , $\tau_{\xi\zeta}$. With attention being restricted to thin shells, terms of order h/R and smaller have been neglected as compared with one, and σ_ζ is neglected compared with the other stresses.

Considering the normal equilibrium of a shell element, (figure 1.2), the following forms of the stress resultants and couples are defined. The stress resultants are

$$N_\xi = \int_{-h/2}^{h/2} \sigma_\xi \, d\zeta$$

$$N_\theta = \int_{-h/2}^{h/2} \sigma_\theta \, d\zeta$$

$$Q = \int_{-h/2}^{h/2} \tau_{\xi\zeta} \, d\zeta$$

and the couples are

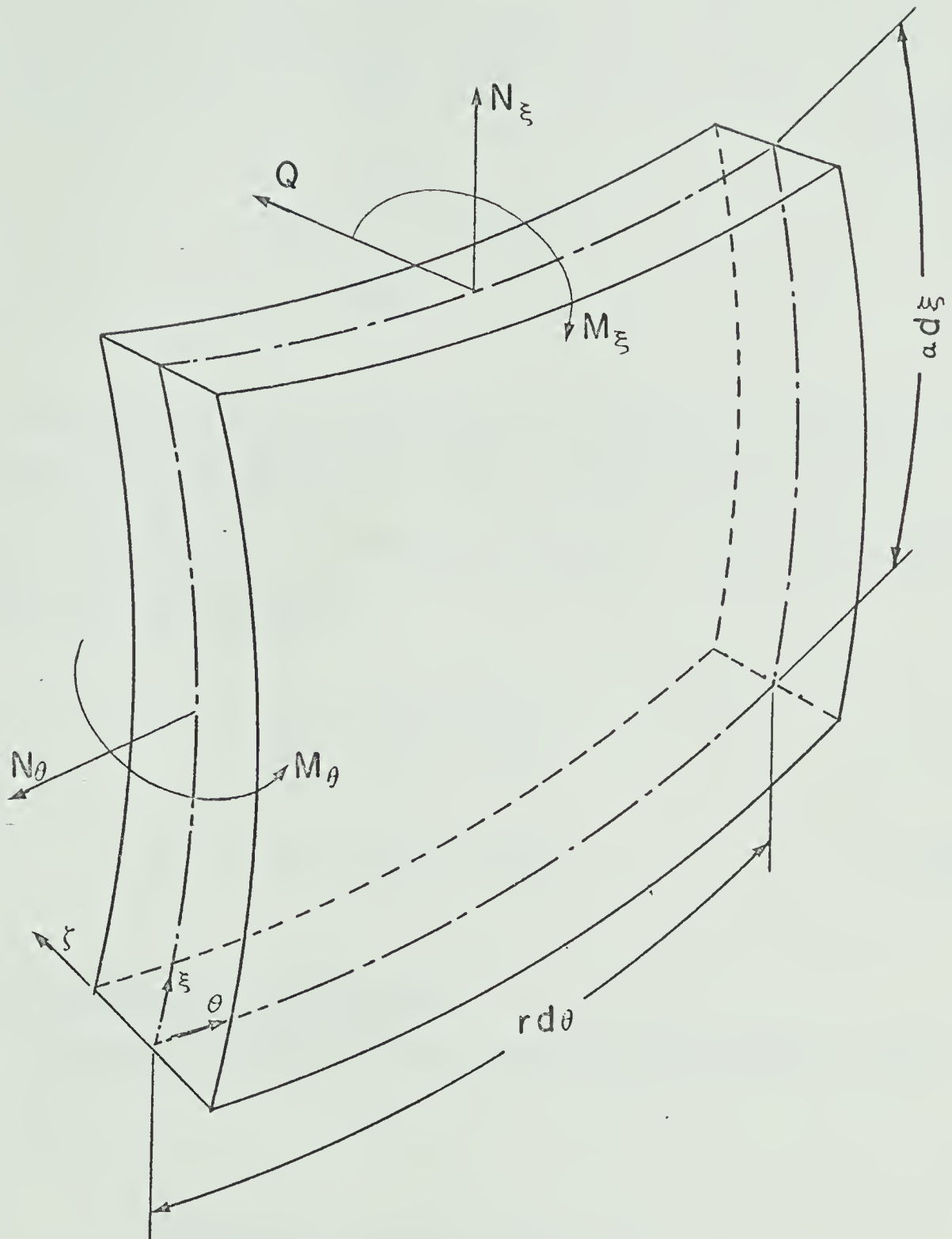


FIGURE 1.2 EQUILIBRIUM OF SHELL ELEMENT

$$M_{\xi} = \int_{-h/2}^{h/2} \sigma_{\xi} \zeta d\zeta \quad (1.15)$$

$$M_{\theta} = \int_{-h/2}^{h/2} \sigma_{\theta} \zeta d\zeta .$$

For convenience the same notation as Reissner's [4] will be employed where a radial (horizontal) stress resultant H and an axial (vertical) stress resultant V have been introduced. These are related to N_{ξ} and Q in the following way:

$$N_{\xi} = H \cos \phi + V \sin \phi \quad (1.16a)$$

$$Q = - H \sin \phi + V \cos \phi . \quad (1.16b)$$

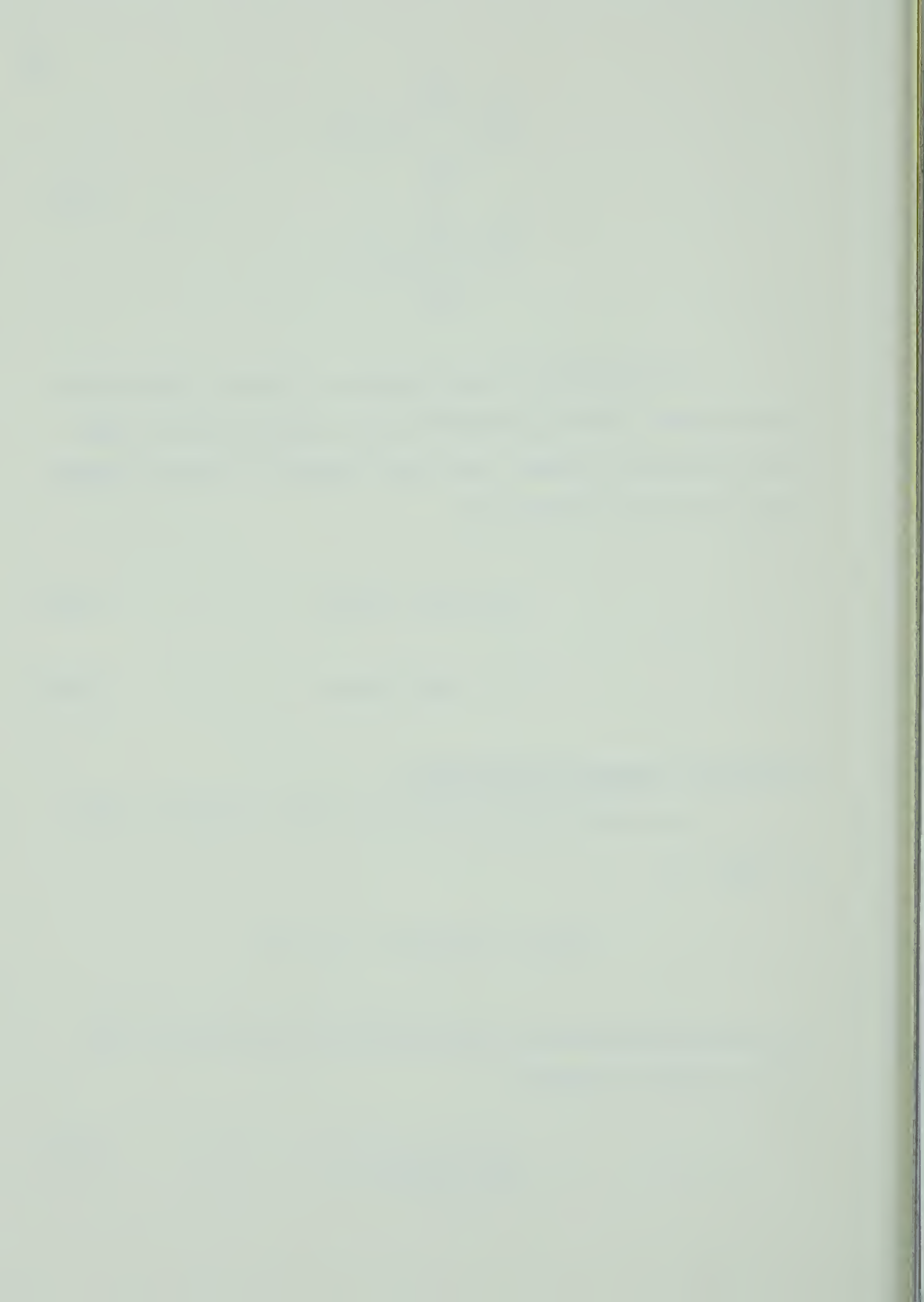
Differential Equations of Equilibrium

We consider the equilibrium in the axial direction as shown in figure 1.2;

$$(r(N_{\xi} \sin \phi + Q \cos \phi))' + p_v r \alpha = 0$$

upon substituting equations (1.16a) and (1.16b), the equilibrium in the axial direction is given by:

$$(rV)' + p_v r \alpha = 0 . \quad (1.17)$$



Similarly, the equation for the equilibrium in the radial direction and the equation due to the moments about a circumferential line are

$$(rH)' - N_{\theta}\alpha + p_H r\alpha = 0 \quad (1.18)$$

and

$$(M_{\xi}r)' + r\alpha(H\sin\phi - V\cos\phi) - M_{\theta}\alpha\cos\phi = 0 \quad (1.19)$$

Stress-Strain Relations

Since σ_{ζ} is neglected as compared with the remaining stresses, the following relationships, derived from Hooke's law, hold,

$$E\varepsilon_{\xi} = \sigma_{\xi} - \nu\sigma_{\theta}$$

$$E\varepsilon_{\theta} = \sigma_{\theta} - \nu\sigma_{\xi}$$

where E is Young's modulus of elasticity and ν is Poisson's ratio.

Inverting these equations, the stresses can be written in terms of the strains as follows,

$$(1-\nu^2)\sigma_{\xi} = E(\varepsilon_{\xi} + \nu\varepsilon_{\theta}) \quad (1.20)$$

$$(1-\nu^2)\sigma_{\theta} = E(\varepsilon_{\theta} + \nu\varepsilon_{\xi})$$



The strains anywhere in the shell may be expressed in terms of the strain along the middle surface plus the strain due to the change in the curvature. The strains at level ζ are given by

$$\epsilon_{\xi} = \epsilon_{\xi M} + \zeta \kappa_{\xi} \quad (1.21)$$

$$\epsilon_{\theta} = \epsilon_{\theta M} + \zeta \kappa_{\theta}$$

Using equations (1.15), (1.20) and (1.21), it can be easily shown that

$$C\epsilon_{\xi M} = N_{\xi} - \nu N_{\theta}$$

$$C\epsilon_{\theta M} = N_{\theta} - \nu N_{\xi}$$

(1.22)

$$M_{\xi} = D(\kappa_{\xi} + \nu \kappa_{\theta})$$

$$M_{\theta} = D(\kappa_{\theta} + \nu \kappa_{\xi})$$

where

$$C = Eh \quad D = \frac{Eh^3}{12(1-\nu^2)} \quad .$$

Equations (1.22), (1.19), (1.18) and (1.17) represent a complete system of seven equations that can be solved for the seven quantities u , β , H , V , N_{θ} , M_{ξ} , M_{θ} .

Equations for Small Deflection

The small deflection theory follows from the differential equations of equilibrium, together with the equations of the stress resultants and by neglecting all non-linear terms in the expressions for the strains. The resulting system of equations can be reduced to two simultaneous second order differential equations with the basic variables β and $(r_0 H)$. In terms of these variables, the system of equations become,

$$r_0 V = - \int r_0 \alpha_0 p_V d\xi \quad (1.23)$$

$$r_0 N_\xi = (r_0 H) \cos \phi_0 + (r_0 V) \sin \phi_0 \quad (1.24)$$

$$r_0 Q = - (r_0 H) \sin \phi_0 + (r_0 V) \cos \phi_0 \quad (1.25)$$

$$\alpha_0 N_\theta = (r_0 H)' + r_0 \alpha_0 p_H \quad (1.26)$$

$$\alpha_0 M_\xi = D(\beta' + \nu(r_0'/r_0)\beta) \quad (1.27)$$

$$\alpha_0 M_\theta = D((r_0'/r_0)\beta + \nu\beta') \quad (1.28)$$

$$u = (r_0/C)(N_\theta - \nu N_\xi) \quad (1.29)$$

$$w = \int \{(z_0'/C)(N_\xi - \nu N_\theta) - r_0'/\beta\} d\xi \quad (1.30)$$

The first of the two simultaneous differential equations for

β and $r_0 H$ is obtained by introducing the moments M_ξ and M_θ from equations (1.27) and (1.28) into the moment equilibrium equation (1.19) for the middle surface. Assuming that the stiffness factors C and D are constant the equation becomes,

$$\begin{aligned} \beta'' + \frac{(r_0/\alpha_0)'}{(r_0/\alpha_0)} \beta' - \left\{ \left(\frac{r_0'}{r_0} \right)^2 - \nu \frac{(r_0'/\alpha_0)'}{(r_0/\alpha_0)} \right\} \beta \\ + \frac{z_0' (r_0 H)}{(r_0 D/\alpha_0)} = \frac{r_0' (r_0 V)}{(r_0 D/\alpha_0)} \quad . \quad \text{I} \end{aligned}$$

In a similar manner, the second differential equation is derived by introducing the strains $\epsilon_{\xi M}$ and $\epsilon_{\theta M}$ from the set of equations (1.22) along with N_ξ and N_θ from equations (1.24) and (1.26) into the compatibility equation (1.14).

$$\begin{aligned} (r_0 H)'' + \frac{(r_0/\alpha_0)'}{(r_0/\alpha_0)} (r_0 H)' - \left\{ (r_0'/r_0)^2 \right. \\ \left. + \nu \frac{(r_0'/\alpha_0)'}{(r_0/\alpha_0)} \right\} (r_0 H) - \frac{z_0'}{(r_0/\alpha_0 C)} \beta \\ = - \left\{ \left[\frac{(r_0/\alpha_0)'}{(r_0/\alpha_0)} + \nu (r_0'/r_0) \right] (r_0 \alpha_0 p_H) \right. \\ \left. + (r_0 \alpha_0 p_H)' \right\} + \left\{ z_0' \frac{r_0'}{r_0^2} + \frac{\nu (z_0'/\alpha_0)'}{(r_0/\alpha_0)} \right\} (r_0 V) \\ + \nu (z_0'/r_0) (r_0 V)' \quad \text{II} \end{aligned}$$

Equations I and II completely describe the behavior of any

symmetric shell of revolution where the theory of small deflections is valid.

The type of cross-section to be considered is shown in figure 1.3. Clark [3] has used the parametric equations

$$r = a + b \sin \xi$$

and
$$z = -\bar{c} (\xi - \sin \xi)$$

where
$$\bar{c} = \frac{2c}{\pi-2} \quad |\xi| \leq \frac{\pi}{2}$$

to describe the profile between the points A and B.

Figure 1.4 shows a comparison between the cross section used here and that of a U shape profile for the case $b = 2c$. The difference between the two profiles seems to be negligible as compared to the variations in the shape of a manufactured bellows.

When the only load on the shell is an axial edge load, the overall equation of axial equilibrium shows that V satisfies the equation

$$2\pi r_0 V = P$$

where P is the total axial load and since there is assumed to be no internal or external pressure $p_v = p_H = 0$.

Substituting the quantities r_0 , z_0 and α_0 into the governing differential equations I and II, it can be verified that they reduce to



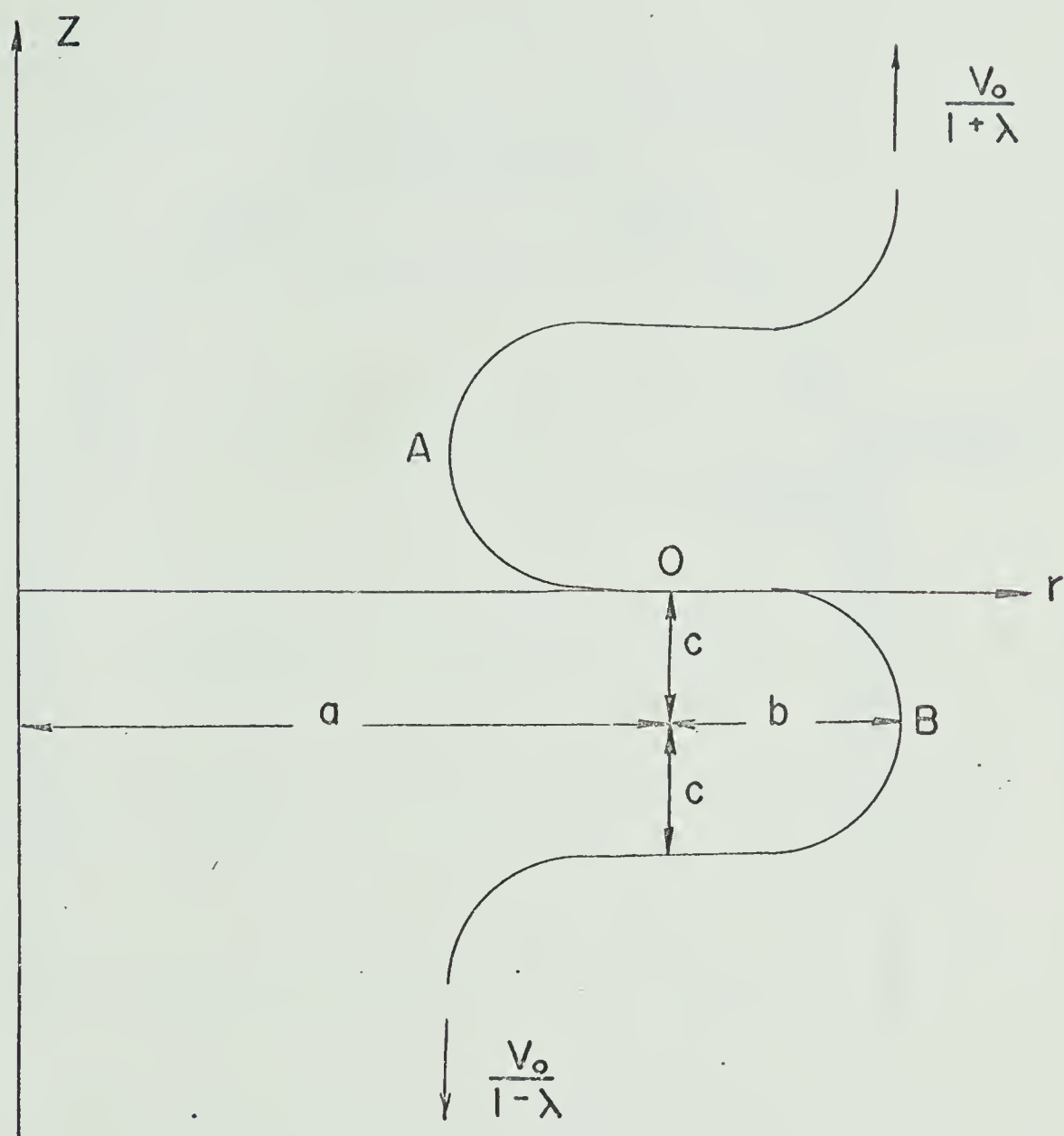


FIGURE 1.3 CROSS - SECTIONAL PROFILE



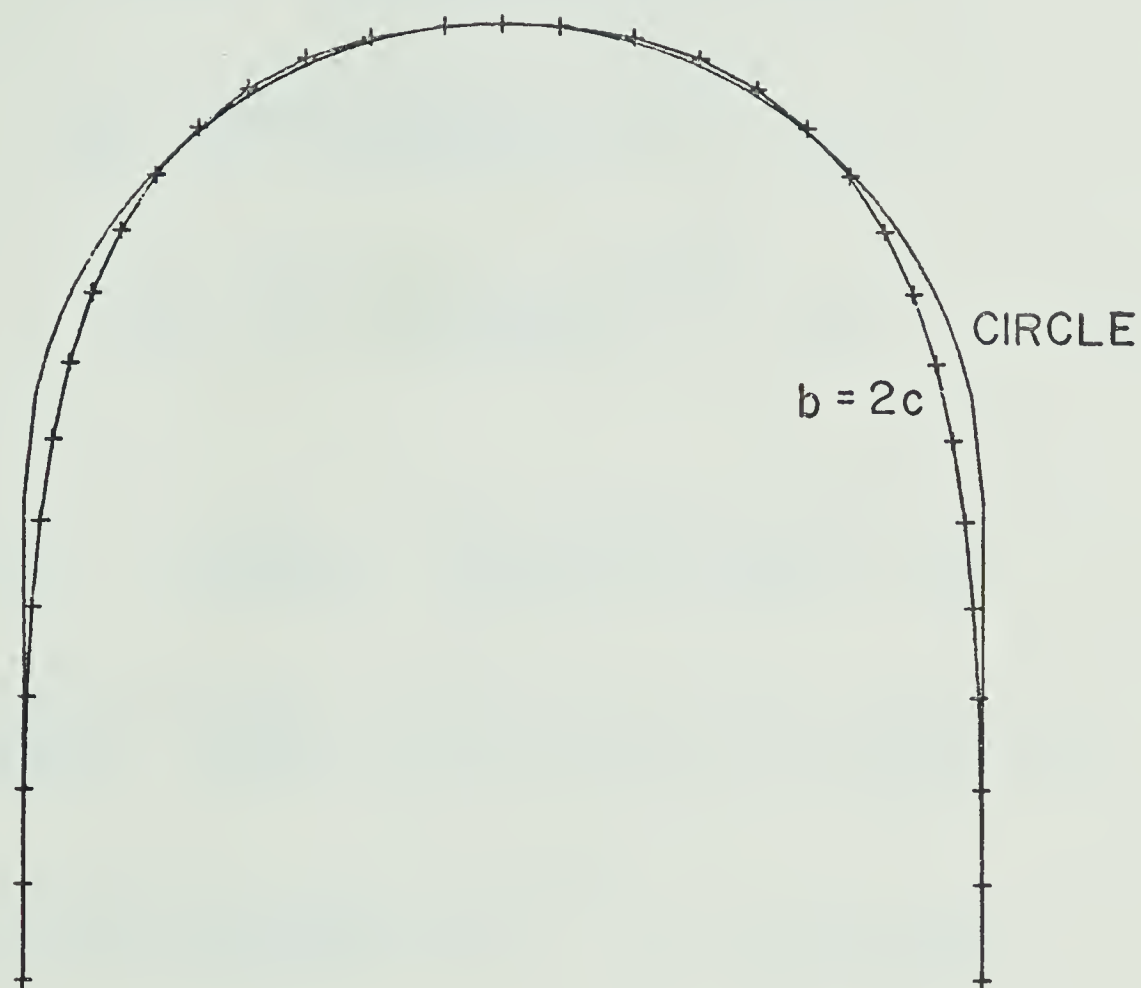


FIGURE 1.4 ASSUMED SHAPE COMPARED
TO A CIRCULAR ARC

the forms.

$$\begin{aligned}
 \beta'' + \left\{ \frac{\lambda \cos \xi}{1 + \lambda \sin \xi} + \frac{\sin \xi (\cos \xi - \eta^2 (1 - \cos \xi))}{(\cos^2 \xi + \eta^2 (1 - \cos \xi)^2)} \right\} \beta' - \left\{ \left(\frac{\lambda \cos \xi}{1 + \lambda \sin \xi} \right)^2 \right. \\
 + \nu \left\{ \frac{\lambda \sin \xi}{1 + \lambda \sin \xi} - \frac{\lambda \cos \xi \sin \xi (\cos \xi - \eta^2 (1 - \cos \xi))}{(\cos^2 \xi + \eta^2 (1 - \cos \xi)^2) (1 + \lambda \sin \xi)} \right\} \beta \\
 \left. - \frac{\bar{c}b}{aD} \frac{(1 - \cos \xi) (\cos^2 \xi + \eta^2 (1 - \cos \xi)^2)^{1/2}}{(1 + \lambda \sin \xi)} \right\} (r_0 H) \\
 = \frac{b^2}{aD} \frac{\cos \xi (\cos^2 \xi + \eta^2 (1 - \cos \xi)^2)^{1/2}}{(1 + \lambda \sin \xi)} (r_0 V) \quad (1.31)
 \end{aligned}$$

and

$$\begin{aligned}
 (r_0 H)'' + \left\{ \frac{\lambda \cos \xi}{(1 + \lambda \sin \xi)} - \frac{\sin \xi (-\cos \xi + \eta^2 (1 - \cos \xi))}{(\cos^2 \xi + \eta^2 (1 - \cos \xi)^2)} \right\} (r_0 H)' \\
 - \left\{ \left(\frac{\lambda \cos \xi}{1 + \lambda \sin \xi} \right)^2 - \frac{\nu \lambda \sin \xi}{1 + \lambda \sin \xi} - \frac{\nu \lambda \cos \xi \sin \xi (-\cos \xi + \eta^2 (1 - \cos \xi))}{(1 + \lambda \sin \xi) (\cos^2 \xi + \eta^2 (1 - \cos \xi)^2)} \right\} (r_0 H) \\
 + \frac{b \bar{c} \bar{c}}{a} \frac{(1 - \cos \xi) (\cos^2 \xi + \eta^2 (1 - \cos \xi)^2)^{1/2}}{(1 + \lambda \sin \xi)} = \frac{\bar{c}}{a} \left\{ \frac{-\lambda (1 - \cos \xi) \cos \xi}{(1 + \lambda \sin \xi)^2} \right. \\
 \left. + \nu \left\{ -\frac{\sin \xi}{(1 + \lambda \sin \xi)} + \frac{(1 - \cos \xi) \sin \xi (-\cos \xi + \eta^2 (1 - \cos \xi))}{(1 + \lambda \sin \xi) (\cos^2 \xi + \eta^2 (1 - \cos \xi)^2)} \right\} \right\} (r_0 V) \quad (1.32)
 \end{aligned}$$

where λ and η have been defined as

$$\lambda = \frac{b}{a} \quad \eta = \frac{\bar{c}}{b}.$$

Equations (1.31) and (1.32) can be solved subject to appropriate

boundary conditions. The four boundary conditions are due to the symmetry conditions of vanishing β and Q for $\xi = \pm \pi/2$. These conditions can be written in the form;

$$\text{at } \xi = \pm \frac{\pi}{2} \quad \beta = 0 \quad (r_o H) = 0 .$$



CHAPTER II

SOLUTION OF EQUATION

2.1 Outer Solution

To determine to what extent the solution of equations (1.31) and (1.32) does not exhibit a boundary layer phenomenon, the dependent variables are non-dimensionalized in the following way,

$$\beta = \beta_0 F(\xi) \quad (r_0 H) = \Psi_0 G(\xi) \quad (r_0 V) = \Psi_0 \quad (2.1)$$

where

$$\Psi_0 = \frac{P}{2\pi} \quad (2.2)$$

Using these non-dimensionalized variables, the two governing differential equations (1.31) and (1.32) become,

$$\begin{aligned} F'' + \left\{ \frac{\lambda \cos \xi}{(1 + \lambda \sin \xi)} + \frac{\sin \xi (\cos^2 \xi + \eta^2 \cos^2 \xi - \eta^2)}{(\cos^2 \xi + \eta^2 (1 - \cos \xi)^2)} \right\} F' \\ - \left[\left(\frac{\lambda \cos \xi}{1 + \lambda \sin \xi} \right)^2 + \frac{\nu \lambda \sin \xi}{(1 + \lambda \sin \xi)} \left\{ 1 + \frac{\cos \xi (-\cos \xi - \eta^2 \cos^2 \xi + \eta^2)}{(\cos^2 \xi + \eta^2 (1 - \cos \xi)^2)} \right\} \right] F \\ - \left[\frac{\bar{c} b \Psi_0}{a D \beta_0} \right] \frac{(1 - \cos \xi) (\cos^2 \xi + \eta^2 (1 - \cos \xi)^2)^{1/2}}{(1 + \lambda \sin \xi)} G \\ = \left[\frac{b^2 \Psi_0}{a D \beta_0} \right] \frac{\cos \xi (\cos^2 \xi + \eta^2 (1 - \cos \xi)^2)^{1/2}}{(1 + \lambda \sin \xi)} \end{aligned} \quad (2.3)$$



$$\begin{aligned}
& G'' + \left\{ \frac{\lambda \cos \xi}{(1+\lambda \sin \xi)} + \frac{\sin \xi (\cos^2 \xi + \eta^2 \cos^2 \xi - \eta^2)}{(\cos^2 \xi + \eta^2 (1 - \cos \xi)^2)} \right\} G' \\
& - \left[\left(\frac{\lambda \cos \xi}{1+\lambda \sin \xi} \right)^2 - \frac{\nu \lambda \sin \xi}{(1+\lambda \sin \xi)} \left\{ 1 + \frac{\cos \xi (-\cos \xi - \eta^2 \cos^2 \xi + \eta^2)}{\cos^2 \xi + \eta^2 (1 - \cos \xi)^2} \right\} \right] G \\
& + \left[\frac{C b \bar{c} \beta_0}{a \Psi_0} \right] \frac{(1 - \cos \xi) (\cos^2 \xi + \eta^2 (1 - \cos \xi)^2)^{1/2}}{(1 + \lambda \sin \xi)} F \\
& = \frac{\bar{c}}{a} \left\{ - \frac{\lambda \cos \xi (1 - \cos \xi)}{(1 + \lambda \sin \xi)^2} - \frac{\nu \sin \xi}{1 + \lambda \sin \xi} \left\{ 1 - \frac{(1 - \cos \xi) (-\cos \xi - \eta^2 \cos^2 \xi + \eta^2)}{\cos^2 \xi + \eta^2 (1 - \cos \xi)^2} \right\} \right\} \quad (2.4)
\end{aligned}$$

Since we are free to choose β_0 , the coefficients of the coupling terms are equated to a new parameter μ

$$\mu = \frac{\bar{c} b \Psi_0}{a D \beta_0} = \frac{C b \bar{c} \beta_0}{a \Psi_0} \quad (2.5)$$

From (2.2) and (2.5), it follows that

$$\beta_0 = \frac{\bar{c} b P}{2 \pi a \mu D} = \frac{\mu a P}{2 \pi b \bar{c} C} \quad (2.6)$$

$$\mu = \frac{\bar{c} b}{a} \left(\frac{C}{D} \right)^{1/2} = [12(1 - \nu^2)]^{1/2} \frac{\bar{c} b}{a h} \quad (2.7)$$

The differential equations (2.3) and (2.4) now become

$$\begin{aligned}
& F'' + \left\{ \frac{\lambda \cos \xi}{(1+\lambda \sin \xi)} + \frac{\sin \xi (\cos^2 \xi + \eta^2 \cos^2 \xi - \eta^2)}{(\cos^2 \xi + \eta^2 (1 - \cos \xi)^2)} \right\} F' \\
& - \left[\left(\frac{\lambda \cos \xi}{1+\lambda \sin \xi} \right)^2 + \frac{\nu \lambda \sin \xi}{(1+\lambda \sin \xi)} \left\{ 1 + \frac{\cos \xi (-\cos \xi - \eta^2 \cos^2 \xi + \eta^2)}{(\cos^2 \xi + \eta^2 (1 - \cos \xi)^2)} \right\} \right] F
\end{aligned}$$

$$- \frac{\mu(1-\cos\xi)(\cos^2_{\xi+\eta}(1-\cos\xi)^2)^{1/2}}{(1+\lambda\sin\xi)} G = \frac{\mu\cos\xi(\cos^2_{\xi+\eta}(1-\cos\xi)^2)^{1/2}}{\eta(1+\lambda\sin\xi)} \quad (2.8)$$

$$\begin{aligned} G'' + \left\{ \frac{\lambda\cos\xi}{1+\lambda\sin\xi} + \frac{\sin\xi(\cos^2_{\xi+\eta}\cos\xi-\eta^2)}{(\cos^2_{\xi+\eta}(1-\cos\xi)^2)} \right\} G' \\ - \left[\left(\frac{\lambda\cos\xi}{1+\lambda\sin\xi} \right)^2 - \frac{\nu\lambda\sin\xi}{(1+\lambda\sin\xi)} \left\{ 1 - \frac{\cos\xi(\cos^2_{\xi+\eta}\cos\xi-\eta^2)}{(\cos^2_{\xi+\eta}(1-\cos\xi)^2)} \right\} \right] G \\ + \frac{\mu(1-\cos\xi)(\cos^2_{\xi+\eta}(1-\cos\xi)^2)^{1/2}}{(1+\lambda\sin\xi)} F \\ = - \frac{\eta\lambda}{(1+\lambda\sin\xi)} \left\{ \frac{\lambda\cos\xi(1-\cos\xi)}{(1+\lambda\sin\xi)} + \nu\sin\xi \right. \\ \left. \left\{ 1 + \frac{(1-\cos\xi)(\cos^2_{\xi+\eta}\cos\xi-\eta^2)}{(\cos^2_{\xi+\eta}(1-\cos\xi)^2)} \right\} \right\} \end{aligned} \quad (2.9)$$

with the boundary conditions

$$\text{at } \xi = \pm \frac{\pi}{2}, \quad F = 0 \quad G = 0.$$

Expressions for the stress resultants and stress couples, in terms of $F(\xi)$ and $G(\xi)$ are obtained from the solution of equations (2.8) and (2.9)

$$N_{\xi} = \frac{P}{2\pi a(1+\lambda\sin\xi)} \{G\cos\xi + \sin\xi\} \quad (2.10)$$

$$N_{\theta} = \frac{P}{2\pi b(\cos^2_{\xi+\eta}(1-\cos\xi)^2)^{1/2}} G' \quad (2.11)$$

$$M_{\xi} = \frac{P\eta\lambda}{2\pi\mu(\cos^2_{\xi+\eta}(1-\cos\xi)^2)^{1/2}} \left\{ F' + \frac{\nu\lambda\cos\xi}{(1+\lambda\sin\xi)} F \right\} \quad (2.12)$$

$$M_{\theta} = \frac{P\eta\lambda}{2\pi\mu(\cos^2_{\xi+\eta}(1-\cos\xi)^2)^{1/2}} \left\{ \frac{\lambda\cos\xi}{1+\lambda\sin\xi} F + \nu F' \right\} . \quad (2.13)$$

For a solution to equations (2.8) and (2.9) to exist, valid throughout the interval $-\pi/2 < \xi < \pi/2$, the parameter μ would have to be of order of unity. This can be seen from equation (2.8), for as μ becomes large compared to unity, the asymptotic solution for $G(\xi)$ is given by

$$G(\xi) \sim - \frac{\cos\xi}{1-\cos\xi}$$

which has a singular point at $\xi = 0$. With μ of order of unity, λ must be small as compared to unity since from equation (2.7) $\lambda/\mu = (h/\bar{c})/[12(1-\nu^2)]^{1/2}$, which is always small when compared to unity. Neglecting terms in λ as compared to the remaining terms, equations (2.8) and (2.9) become

$$\begin{aligned} & F'' + \frac{\sin\xi(\cos^2_{\xi+\eta}\cos\xi-\eta^2)}{(\cos^2_{\xi+\eta}(1-\cos\xi)^2)} F' \\ & - \mu(1-\cos\xi)(\cos^2_{\xi+\eta}(1-\cos\xi)^2)^{1/2} G \\ & = \frac{\mu}{\eta} \cos\xi(\cos^2_{\xi+\eta}(1-\cos\xi)^2)^{1/2} \end{aligned} \quad (2.14)$$

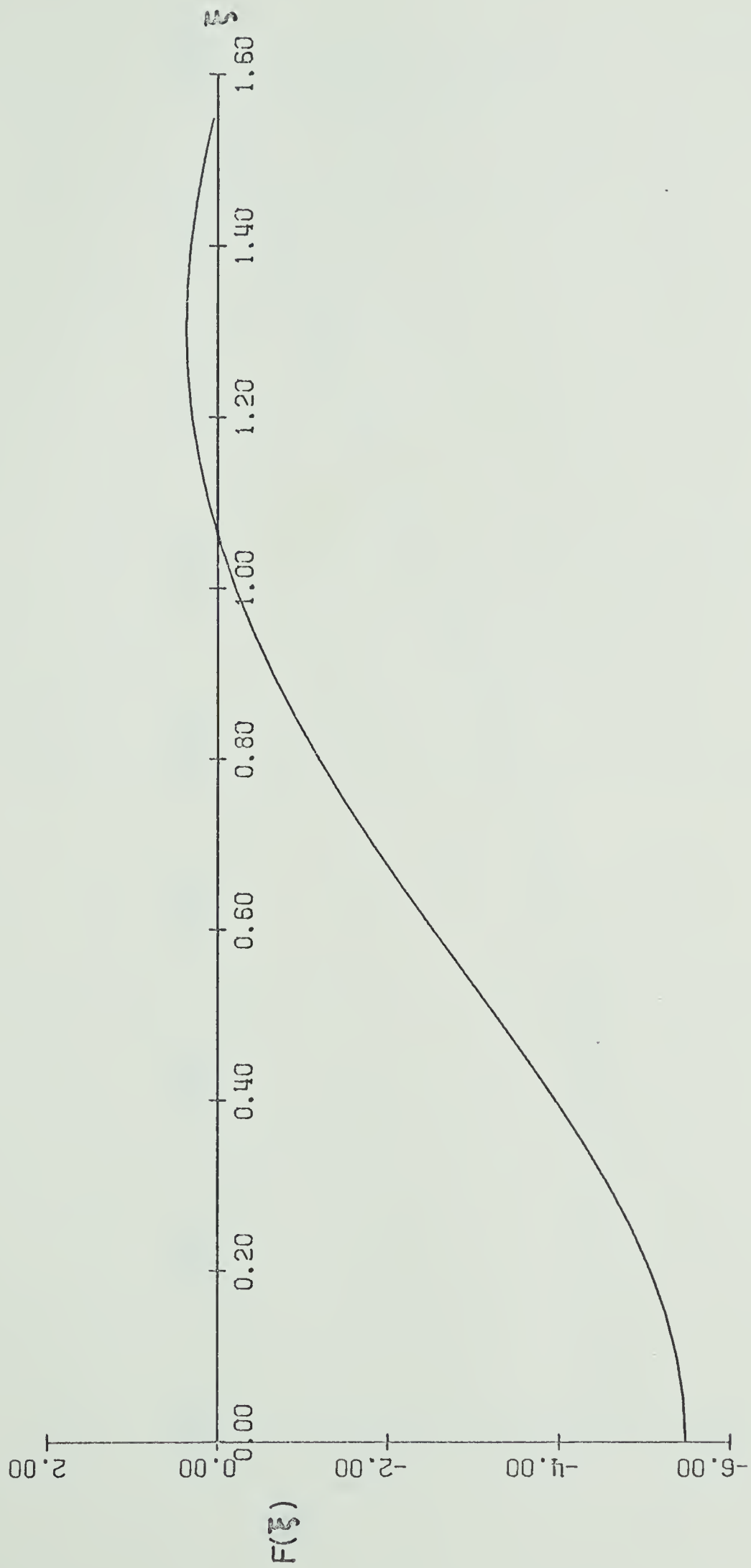


FIGURE 2.1 DEPENDENT VARIABLE F

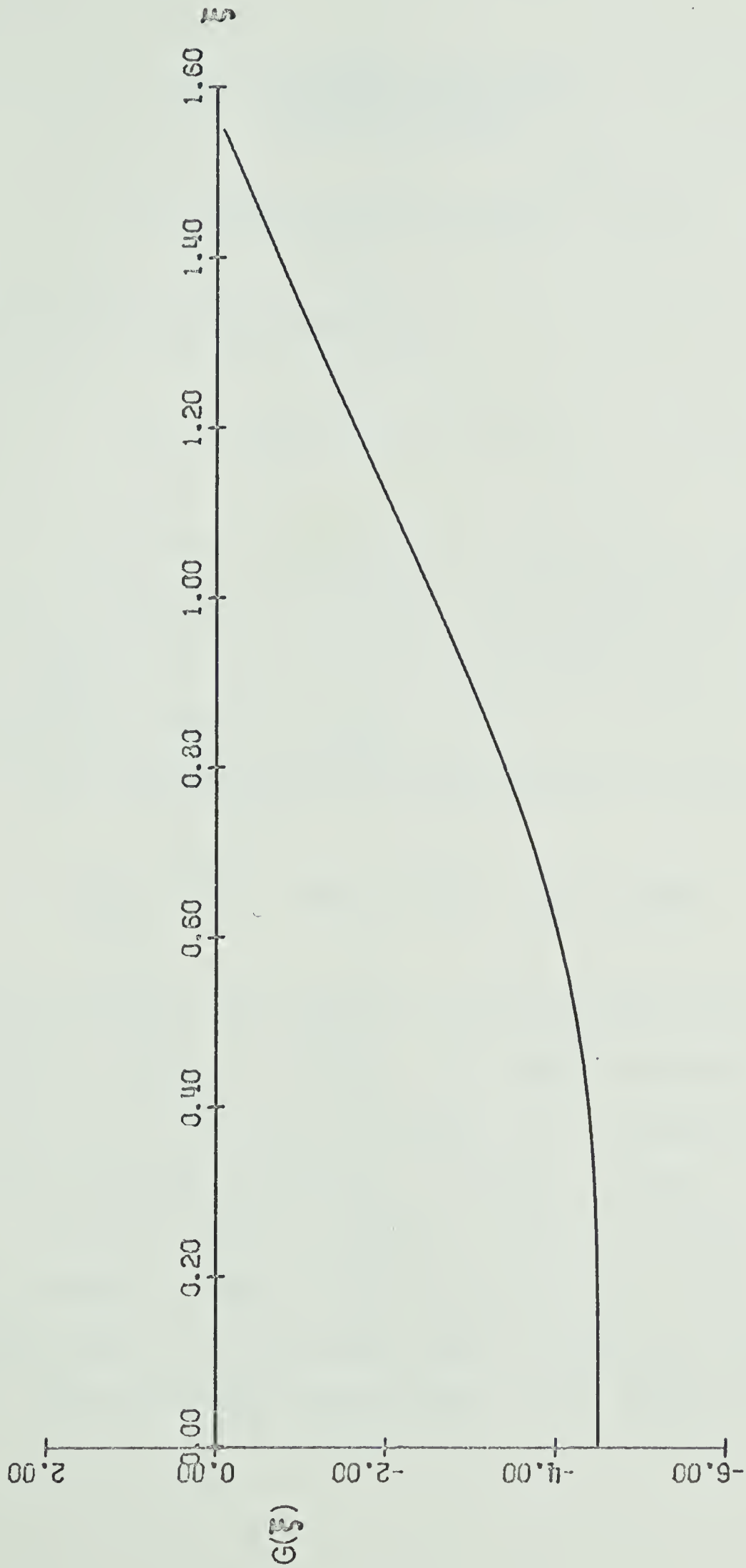


FIGURE 2.2 DEPENDENT VARIABLE G

$$\begin{aligned}
& G'' + \frac{\sin \xi (\cos^2 \xi + \eta^2 \cos^2 \xi - \eta^2)}{\cos^2 \xi + \eta^2 (1 - \cos \xi)^2} G' \\
& + \mu (1 - \cos \xi) (\cos^2 \xi + \eta^2 (1 - \cos \xi)^2)^{1/2} F = 0 \quad (2.15)
\end{aligned}$$

together with the boundary conditions

$$\text{at } \xi = \pm \frac{\pi}{2} \quad F = 0 \quad G = 0 \quad .$$

It should be noted here, that as μ becomes large compared with unity, the equations are no longer valid near the origin. In addition, although λ/μ is always small compared with one, the value of λ is no longer necessarily small.

For an approximation to the outer solution for the case

$$b/a = 0.2117 \quad c/b = 0.6257 \quad h/a = 0.0069$$

equations (2.14) and (2.15) have been solved numerically with $F(\xi)$ and $G(\xi)$ plotted in figures 2.1 and 2.2. This example corresponds to the experimental bellow that is used in Chapter III. The geometric values given above correspond to the case $\mu = 11.7640$, $\lambda = 0.2117$.

The radial stresses are shown in figure 2.3 and the circumferential stresses in figure 2.4 for a compressive load. The values are not valid near $\xi = 0$, but become closer to the actual stresses as $\xi \rightarrow \pm \frac{\pi}{2}$. The outer solution obtained here will be matched up with

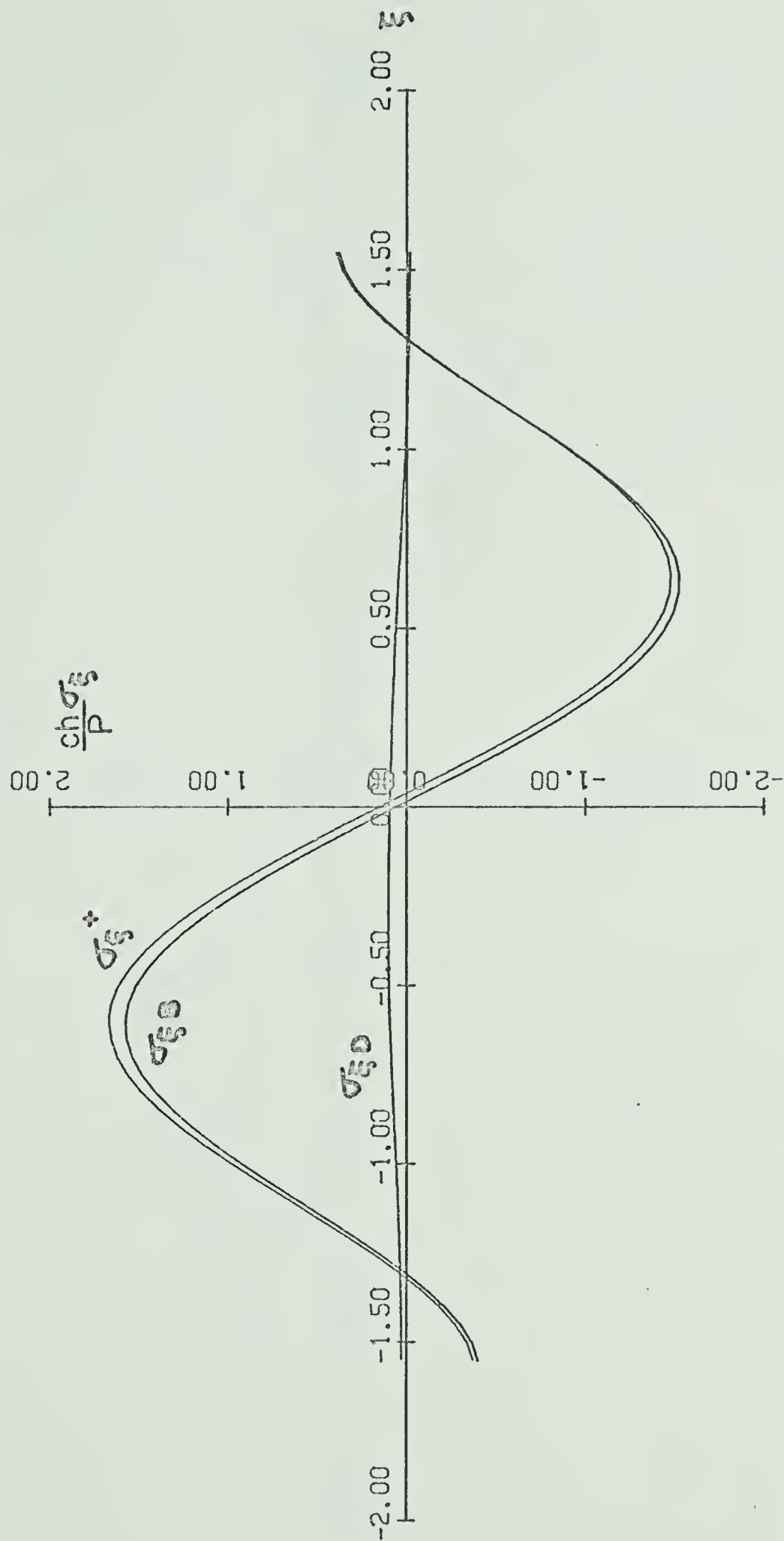


FIGURE 2.3 RADIAL STRESSES

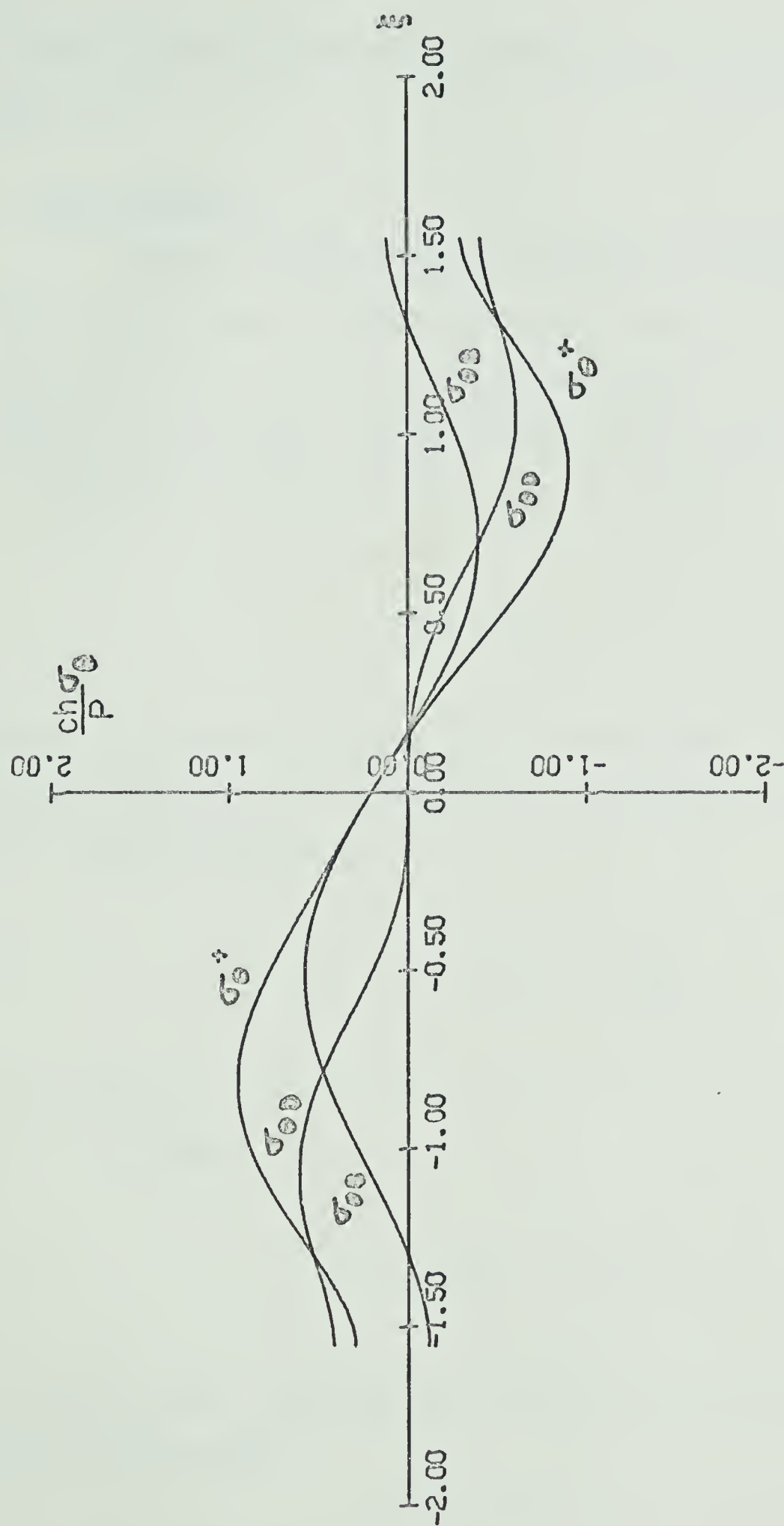


FIGURE 2.4 CIRCUMFERENTIAL STRESSES

the inner solution to give a more accurate solution throughout the range of ξ .

2.2 Inner Solution

From the structure of the differential equations (2.8) and (2.9), it can be seen that when μ is large compared to unity, the neighborhood of $\xi = 0$ is an area of rapid changes in the dependent variables $F(\xi)$ and $G(\xi)$. For the analysis of the inner solution a new independent variable ρ is introduced in the form

$$\rho = \tau \xi$$

where $\tau \gg 1$ such that a narrow region surrounding $\xi = 0$ becomes a region surrounding $\rho = 0$. Since we are considering the neighborhood of $\xi = 0$ the approximations

$$\sin \xi = \frac{\rho}{\tau} \quad \cos \xi = 1 - \frac{\rho^2}{2\tau^2}$$

will be used.

Defining

$$F = F_0 f(\rho) \quad G = G_0 g(\rho)$$

and using the above approximations, the governing differential equations (2.8) and (2.9) become

$$\left[\frac{\eta\tau^2 F_0}{\mu}\right] f'' + \left[\frac{\eta\tau^2 F_0}{\mu}\right] \frac{\lambda}{\tau} f' - \left[\frac{\eta\tau^2 F_0}{\mu}\right] \frac{\lambda^2}{\tau^2} f - \left[\frac{\eta G_0}{2\tau^2}\right] \rho^2 g = 1 \quad (2.16)$$

$$\left[\frac{\eta\tau^2 G_0}{\mu}\right] g'' + \left[\frac{\eta\tau^2 G_0}{\mu}\right] \frac{\lambda}{\tau} g' - \left[\frac{\eta\tau^2 G_0}{\mu}\right] \frac{\lambda^2}{\tau^2} g + \left[\frac{\eta F_0}{2\tau^2}\right] \rho^2 f = 0 \quad (2.17)$$

Two conditions for the determination of the parameters τ , F_0 and G_0 come from equation (2.16), by requiring that the coefficients of f'' , g and 1 be of comparable magnitude

$$\frac{\eta\tau^2 F_0}{\mu} = \frac{\eta G_0}{2\tau^2} = 1 \quad (2.18)$$

The third condition follows from equation (2.17) by requiring that the terms with g'' and f be of comparable magnitude

$$\frac{\tau^2 G_0}{\mu} = \frac{F_0}{2\tau^2} \quad (2.19)$$

Solving equations (2.18) and (2.19) for the parameters τ , F_0 and G_0 , we have

$$\tau = \left(\frac{\mu}{2}\right)^{1/4} \quad (2.20)$$

$$F_0 = \frac{2}{\eta} \left(\frac{\mu}{2}\right)^{1/2} \quad (2.21)$$

$$G_0 = \frac{2}{\eta} \left(\frac{\mu}{2}\right)^{1/2} \quad (2.22)$$

Using the relationships (2.20) to (2.22) and the fact that $\tau \gg 1$, the two simultaneous differential equations (2.16) and (2.17) can be reduced by neglecting terms of smaller magnitudes

$$f'' - \rho^2 g = 1 \quad (2.23)$$

$$g'' + \rho^2 f = 0 \quad (2.24)$$

with the boundary conditions in the form

$$\text{at } \rho = \pm \infty, \quad f = 0 \quad g = 0$$

It must be noted that the solution of equations (2.23) and (2.24) are valid only if $\tau \gg 1$.

Expressions for the stress resultants and couples follow from equation (2.10) to (2.13) in the form,

$$N_{\xi} = \frac{P}{2\pi a(1+\lambda \sin \xi)} \left\{ \frac{2}{\eta} \left(\frac{\mu}{2}\right)^{1/2} \cos \xi + \sin \xi \right\} \quad (2.25)$$

$$N_{\theta} = \frac{P}{\pi b (\cos^2_{\xi+\eta} (1-\cos \xi)^2)^{1/2} \eta} \left(\frac{\mu}{2}\right)^{3/4} g' \quad (2.26)$$

$$M_{\xi} = \frac{P\lambda}{2\pi (\cos^2_{\xi+\eta} (1-\cos \xi)^2)^{1/2} \left(\frac{\mu}{2}\right)^{1/2}} \left\{ \left(\frac{\mu}{2}\right)^{1/4} f' + \frac{\nu \lambda \cos \xi}{1+\lambda \sin \xi} f \right\} \quad (2.27)$$

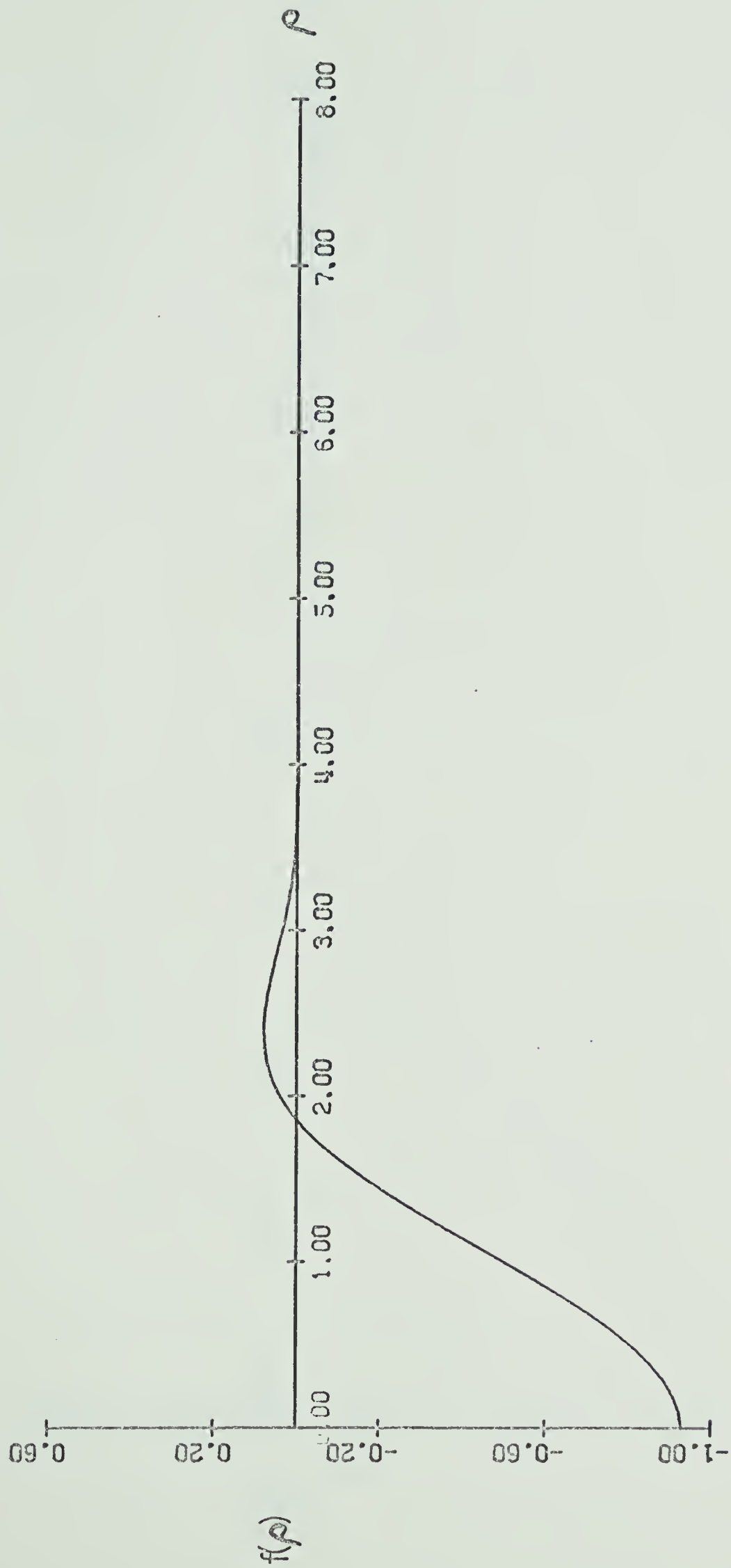


FIGURE 2.5 DEPENDENT VARIABLE f

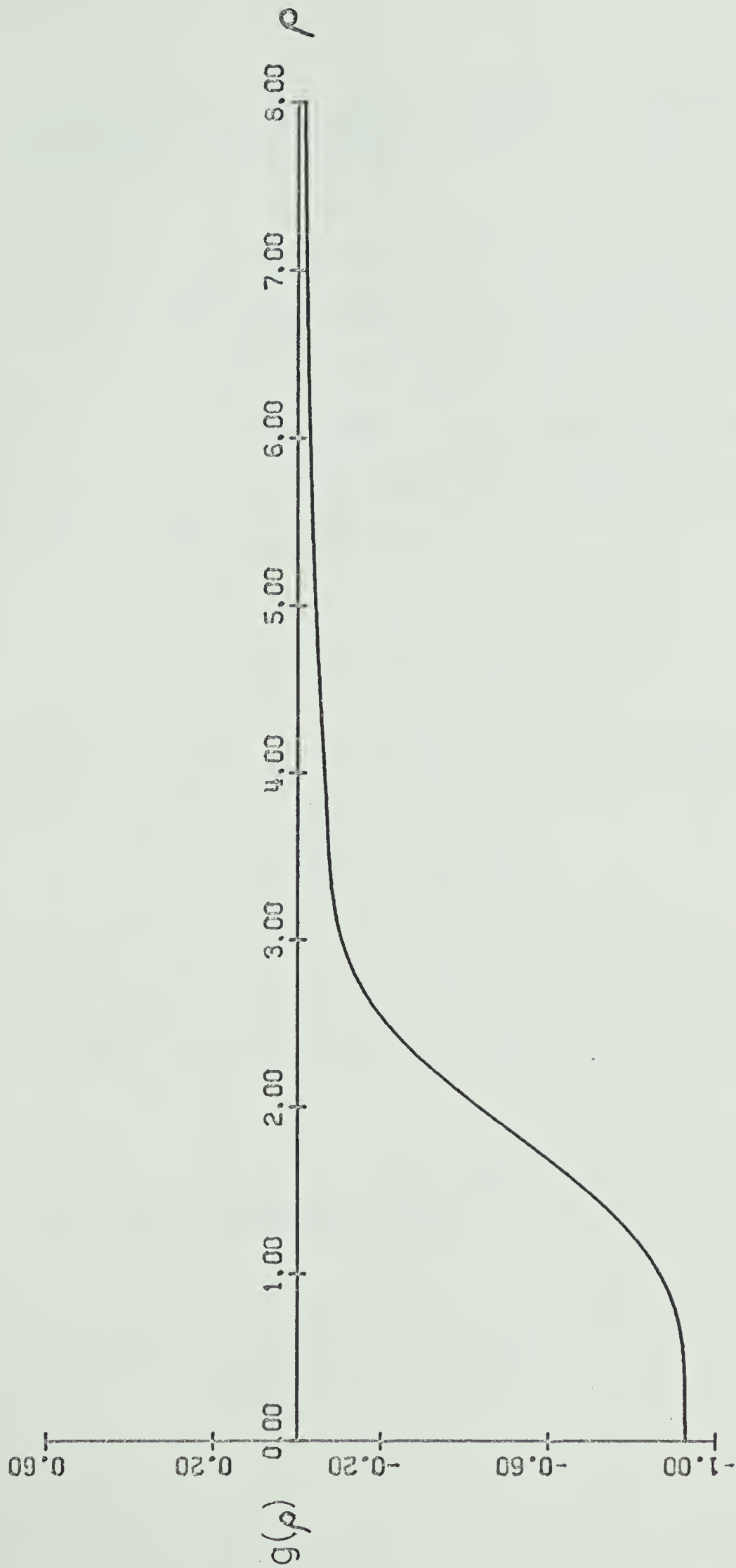


FIGURE 2.6 DEPENDENT VARIABLE g

$$M_{\theta} = \frac{P\lambda}{2\pi(\cos^2\xi + \eta^2(1-\cos\xi)^2)^{1/2}} \frac{1}{(\mu/2)^{1/2}} \left\{ \frac{\lambda\cos\xi}{1+\lambda\sin\xi} f + \nu\left(\frac{\mu}{2}\right)^{1/4} \right\} f' \quad (2.28)$$

The total stress in the surface fibers of the shell can be written as the sum of the direct membrane stress and the stress due to bending, $\sigma = \sigma_D \mp \sigma_B$. The upper sign refers to the surface which is farthest from the axis of revolution, while the lower sign refers to the surface closest to the axis of revolution. The direct stresses are related to the stress resultants by

$$\sigma_{\xi D} = \frac{N_{\xi}}{h} \quad \sigma_{\theta D} = \frac{N_{\theta}}{h} \quad (2.29)$$

while the bending stresses are related to the stress couples by

$$\sigma_{\xi B} = \frac{6M_{\xi}}{h^2} \quad \sigma_{\theta B} = \frac{6M_{\theta}}{h^2} \quad (2.30)$$

Using equations (2.25) to (2.30), the direct stress and bending stress for both the radial and circumferential directions can be written in the form,

$$\sigma_{\xi D} = \frac{P}{ch} \frac{(\pi-2)\eta\lambda}{4\pi(1+\lambda\sin\xi)} \left\{ \frac{2}{\eta} \left(\frac{\mu}{2}\right)^{1/2} \cos\xi g + \sin\xi \right\} \quad (2.31)$$

$$\sigma_{\theta D} = \frac{P}{ch} \frac{(\pi-2)}{2\pi(\cos^2\xi + \eta^2(1-\cos\xi)^2)^{1/2}} \left(\frac{\mu}{2}\right)^{3/4} g' \quad (2.32)$$

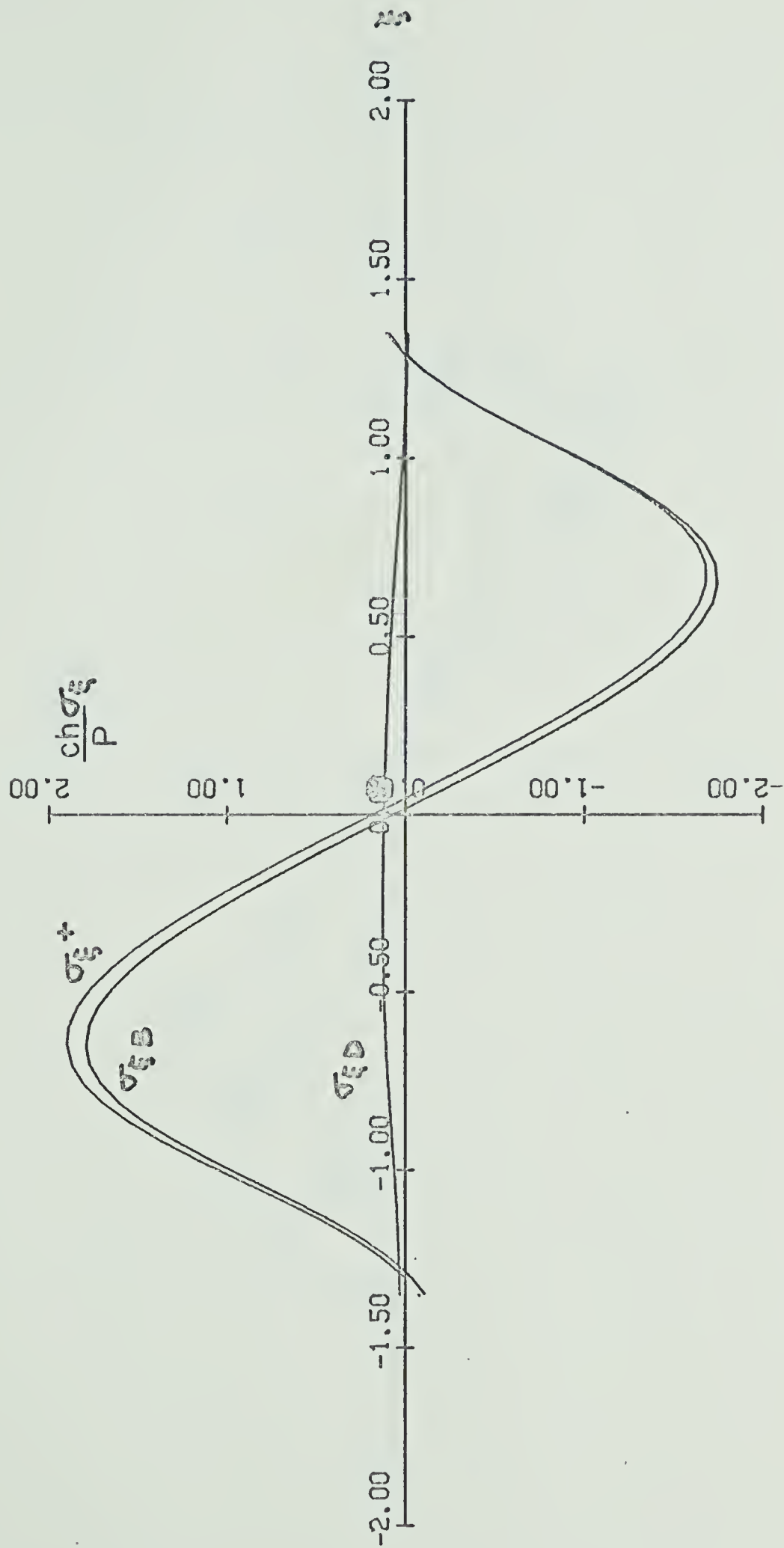


FIGURE 2.7 RADIAL STRESSES

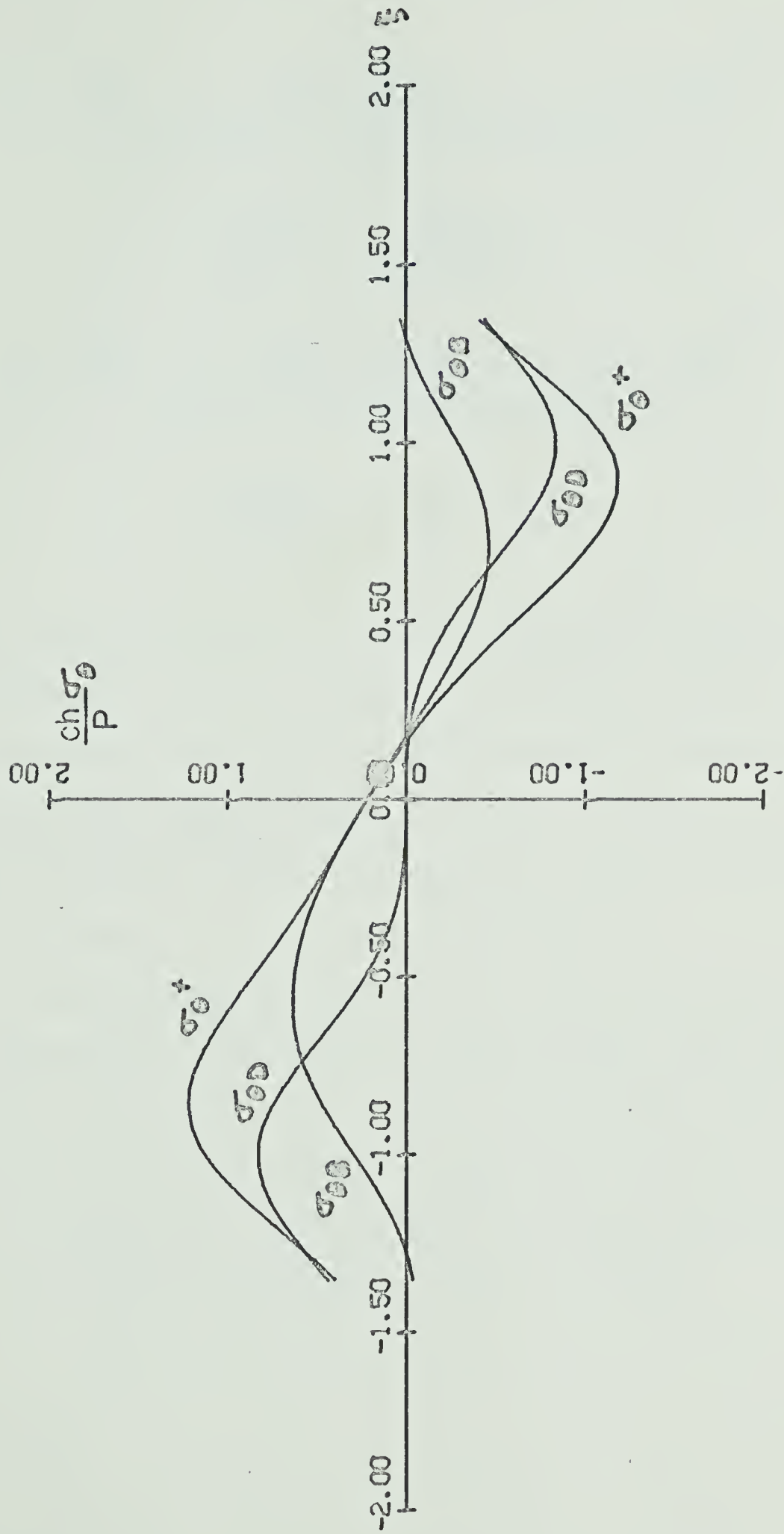


FIGURE 2.8 CIRCUMFERENTIAL STRESSES

$$\sigma_{\xi B} = \frac{P}{ch} \frac{3^{1/2} (\pi-2)}{2\pi(1-\nu^2)^{1/2} (\cos^2 \xi + \eta^2 (1-\cos \xi)^2)^{1/2}} \left(\frac{\mu}{2}\right)^{1/2} \left\{ \left(\frac{\mu}{2}\right)^{1/4} f' + \frac{\nu \lambda \cos \xi f}{1+\lambda \sin \xi} \right\} \quad (2.33)$$

$$\sigma_{\theta B} = \frac{P}{ch} \frac{3^{1/2} (\pi-2)}{2\pi(1-\nu^2)^{1/2} (\cos^2 \xi + \eta^2 (1-\cos \xi)^2)^{1/2}} \left(\frac{\mu}{2}\right)^{1/2} \left\{ \frac{\lambda \cos \xi}{1+\lambda \sin \xi} f + \nu \left(\frac{\mu}{2}\right)^{1/4} f' \right\} \quad (2.34)$$

Equations (2.23) and (2.24) are solved by numerical integration and the functions $f(\rho)$ and $g(\rho)$ are plotted in figures 2.5 and 2.6 respectively. Since the solution of the equations is independent of μ , other than μ being large as compared to unity, the values of $f(\rho)$ and $g(\rho)$ are tabulated in appendix C to be used in determining the stresses in the region near $\xi = 0$ for all U-shaped bellows.

Using the example cited earlier in the outer solution, the stress distribution is solved for the inner solution. The radial direct stress, the radial bending stress and the total radial stress for the inner surface are plotted in figure 2.7. Similarly in figure 2.8, the circumferential direct stress, the circumferential bending stress and the total circumferential stress are plotted.

CHAPTER III

EXPERIMENTAL INVESTIGATION

A manufactured Flexonics expansion joint was purchased for the experimental investigation of the stresses caused by an axial load. The bellow pictured in figure 3.1 is designed to fit a nominal pipe size of eight inches. With three corrugations, it has a maximum axial traverse of one and a half inches. The bellow is manufactured out of stainless steel type 304 and is free flexing in that there is no control on the maximum or minimum traverse travel or angular rotation. The actual contour of the corrugations as shown in figure 3.3, is more of an S-shape profile rather than the shape used earlier in the theoretical analysis.

To determine the values of a , b , c , and h for the bellow considered here a number of readings were taken and the average values used. These readings are recorded in appendix A where the average values are given. A variation of 0.065 inches was found in the depth while a variation of 0.040 inches was found in the width of the corrugations. The readings for the thickness of the material were taken on the end flanges using a micrometer.

Four Budd metalfilm strain gauges (type C6-121) were placed at ninety degrees to each other on each of the three corrugations. The reason for this arrangement was to try to predict if a purely axial load was being applied. Since the loads being applied were in the

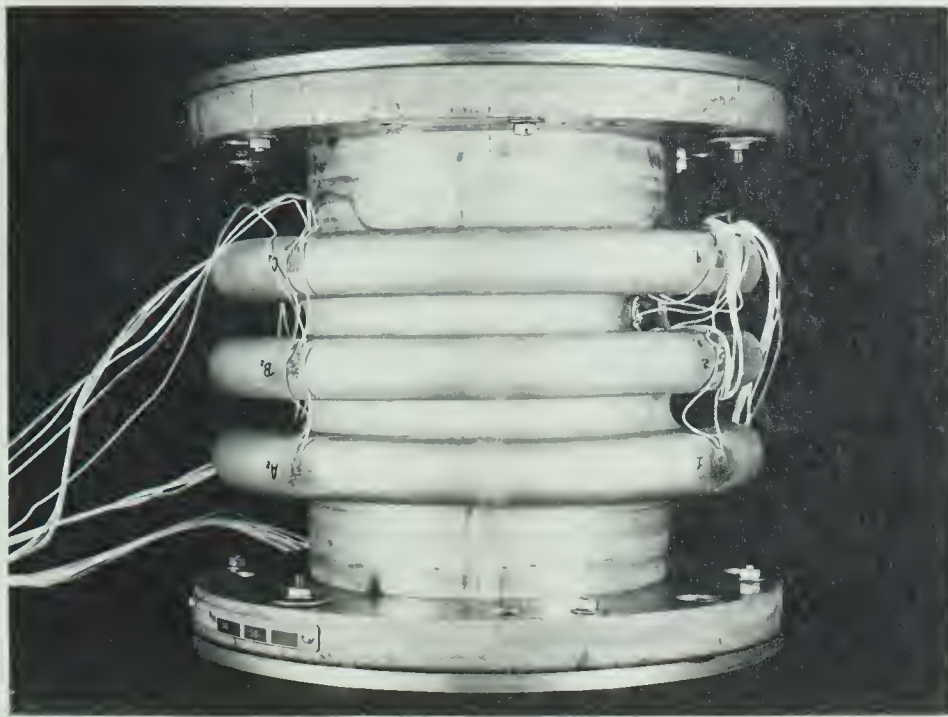


FIG. 3.1 EXPANSION JOINT

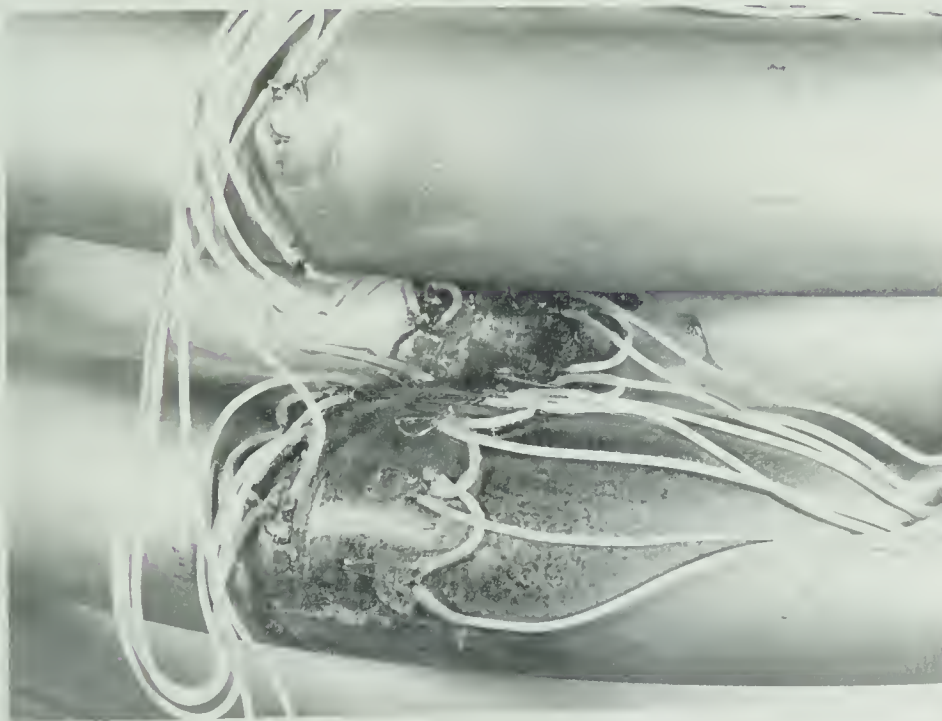


FIG. 3.2 STRAIN GAUGES

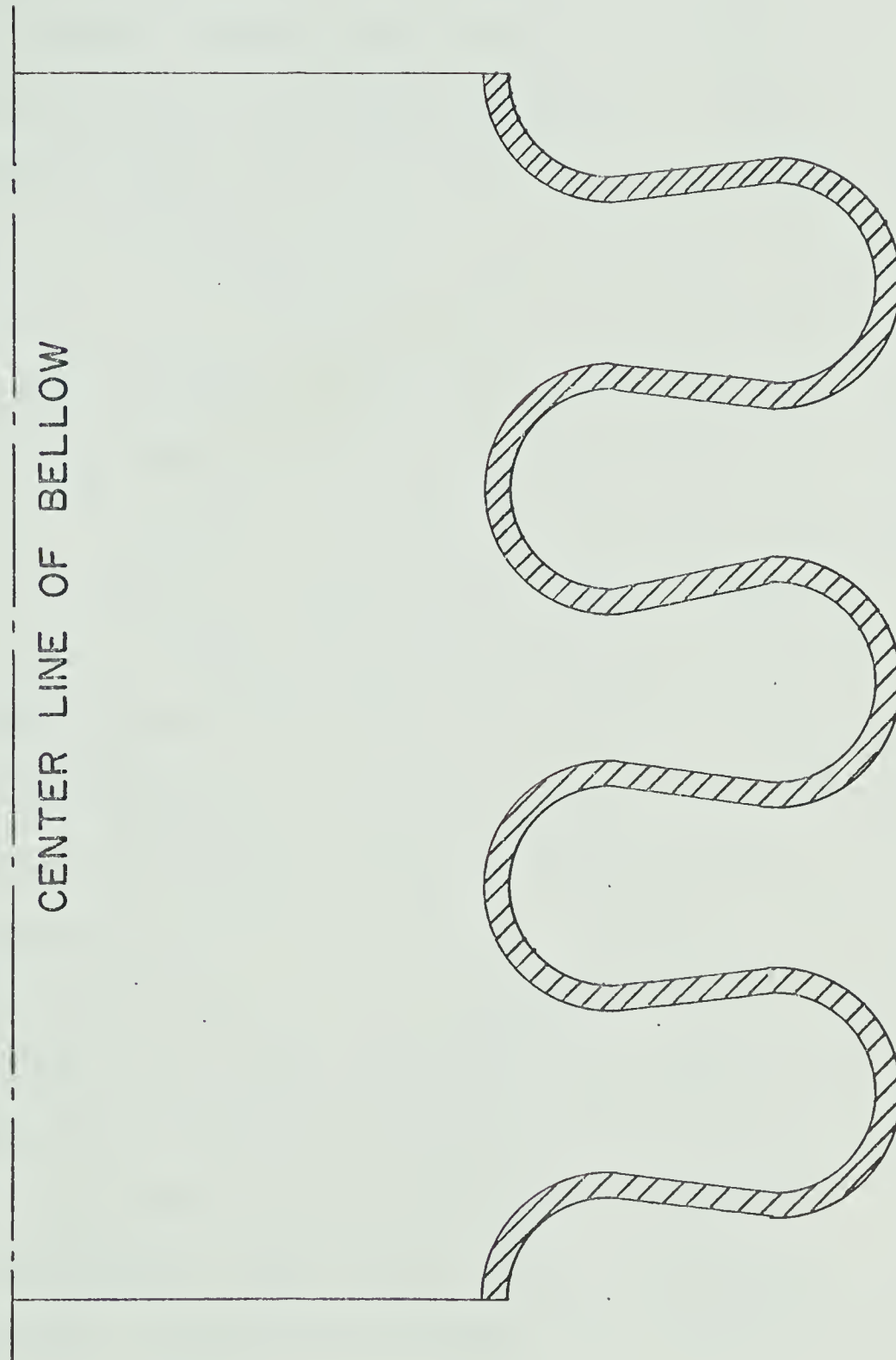


FIGURE 3.3 S SHAPE PROFILE

range from zero to five hundred pounds, the strain at the tips of each corrugation was too small to give any indication as to whether an eccentric load was being applied. To determine the stress distribution along a meridian, fourteen strain gauges were mounted on the outside surface of one half of the middle corrugation as shown in figure 3.2. Grouping the gauges into pairs, one to record the radial strain and one to record the circumferential strain, and equally spacing each pair along a meridian, the complete strain distribution was determined. Opposite the pairs of gauges on the outside surface were mounted another five pairs of gauges to record the strain distribution on the inside surface. In figure 3.4, the location of all the strain gauges is shown and the numbers correspond to the gauges in appendix B.

An Instron testing machine was used for the application of the axial load as shown in figure 3.5. The maximum load range used was five hundred pounds with an accuracy of plus or minus two pounds. Load increments of one hundred pounds were applied and the strains were recorded by using two types of strain indicators - a Baldwin-Lima-Hamilton strain indicator and an Automation Industries strain indicator. Gauges one to seven were hooked to the former while gauges eight to twenty-four, using two switching units, were hooked to the latter. All experimental data has been listed in appendix B.

From equation (1.20), the radial and circumferential stresses can be determined. For comparison purposes, the stresses are written in the dimensionless form

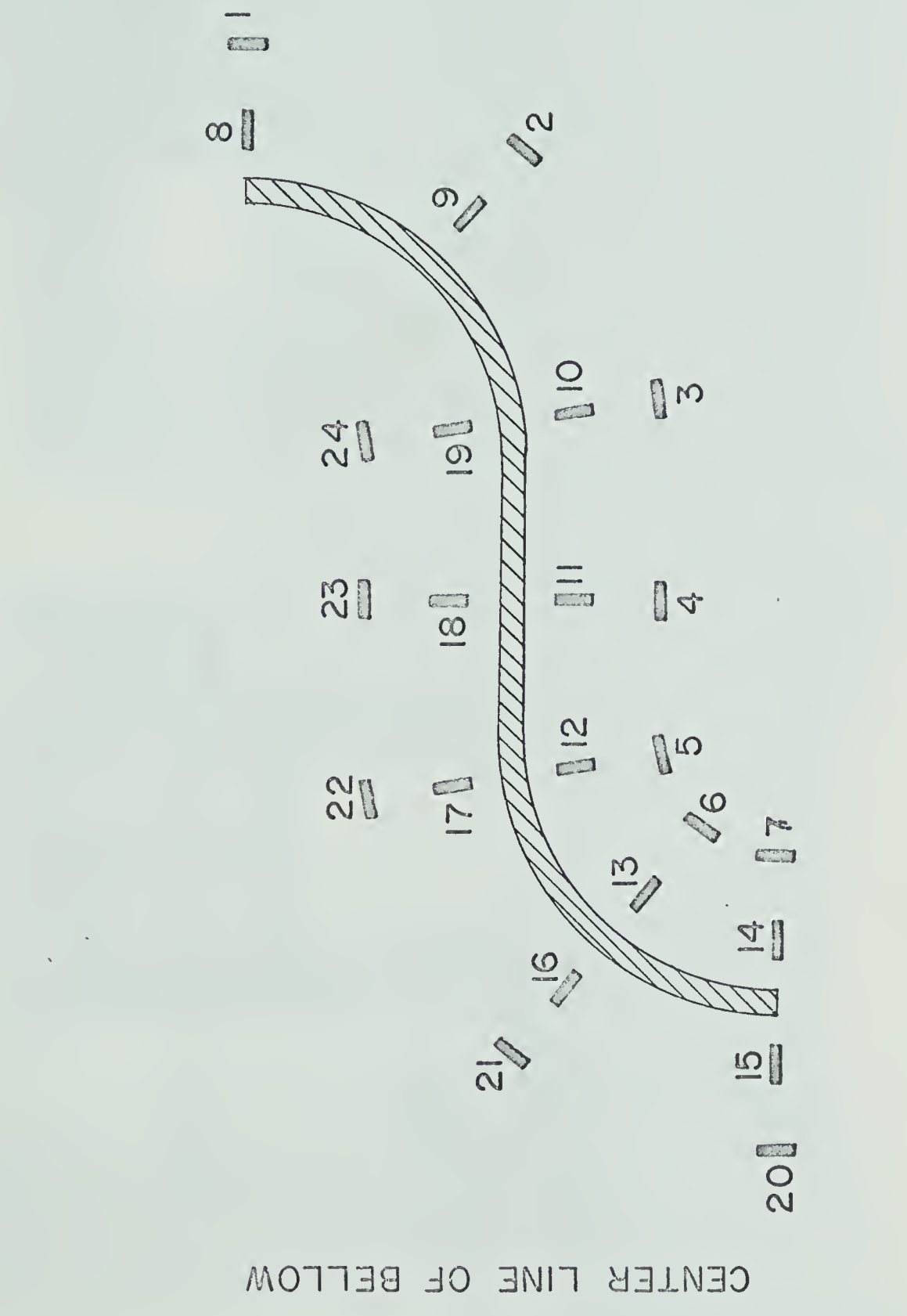


FIGURE 3.4 LOCATION OF STRAIN GAUGES



FIG. 3.5 TEST SET - UP

$$\frac{ch\sigma_{\xi}}{P} = \frac{ch E}{P(1-v^2)} (\epsilon_{\xi} + v\epsilon_{\theta})$$

and

$$\frac{ch\sigma_{\theta}}{P} = \frac{ch E}{P(1-v^2)} (\epsilon_{\theta} + v\epsilon_{\xi})$$

The values $ch \sigma_{\xi}/P$ for the outside radial gauges are listed in table 3.1. Similarly for the outside circumferential, the inside radial, and the inside circumferential gauges, the values of $ch\sigma/P$ are listed in tables 3.2, 3.3 and 3.4 respectively.

Table 3.1
Outside Radial

$\xi(\text{rads})$	ch σ_{ξ}/P				Average
$\pi/2$	0.25	0.25	0.25	0.25	0.25
0.9407	1.28	1.45	1.50	1.50	1.43
0.4555	1.97	2.06	2.04	1.97	2.01
0	-0.12	-0.04	-0.05	-0.10	-0.08
-0.4555	-0.87	-1.09	-1.09	-1.02	-1.02
-0.9407	-2.34	-2.53	-2.47	-2.42	-2.44
$-\pi/2$	-0.74	-0.88	-0.93	-0.97	-0.88

Table 3.2
Outside Circumferential

$\xi(\text{rads})$	ch σ_{θ}/P				Average
$\pi/2$	0.83	0.85	0.85	0.84	0.84
0.9407	0.83	0.87	0.86	0.84	0.85
0.4555	-0.28	-0.29	-0.31	-0.34	-0.31
0	-1.18	-1.16	-1.13	-1.13	-1.15
-0.4555	-0.14	-0.17	-0.15	-0.12	-0.15
-0.9407	-0.40	-0.43	-0.39	-0.37	-0.40
$-\pi/2$	-0.93	-0.95	-0.94	-0.94	-0.94

Table 3.3
Inside Radial

$\xi(\text{rads})$	$\text{ch } \sigma_{\xi}/P$				Average
$-\pi/2$	0.90	0.94	0.96	0.96	0.94
-0.9407	2.34	2.34	2.27	2.21	2.29
-0.4555	1.51	1.50	1.44	1.39	1.46
0	-0.16	-0.06	0.02	0.08	-0.03
0.4555	-1.74	-1.65	-1.54	-1.44	-1.59

Table 3.4
Inside Circumferential

$\xi(\text{rads})$	$\text{ch } \sigma_{\theta}/P$				Average
$-\pi/2$	-0.42	-0.39	-0.36	-0.34	-0.38
-0.9407	1.08	1.11	1.10	1.10	1.10
-0.4555	1.38	1.38	1.34	1.31	1.35
0	-0.54	-0.54	-0.52	-0.50	-0.53
0.4555	-1.11	-1.10	-1.08	-1.06	-1.09

CHAPTER IV

DISCUSSION OF RESULTS

The complete theoretical stress distribution is found by matching the inner and outer solutions. Figures 4.1 and 4.2 show the two solutions superimposed for the radial and circumferential stresses respectively. The complete solution can be broken down into two regions, one where only the inner solution is valid, and one where only the outer solution is valid.

In the interval $\xi \approx \pm 0.40$, the deviations of the outer solution from the inner solution become negligible. This is more likely a coincidence since for large values of μ , the outer solution is not valid near $\xi = 0$. As ξ increases from ± 0.40 to ± 1.20 , the variation between the two solutions increases to a maximum near $\xi = \pm 0.65$.

Throughout this region the inner solution is valid, while for ξ greater than ± 1.20 , the outer solution becomes valid. The matching of the inner and outer solutions produces a relatively continuous solution for the stress distribution in the expansion joint.

For a qualitative view of the theory developed here, the experimental values from Chapter III and the results of Clark [3] are used for comparison.

In figure 4.3, both the inside and the outside radial stress

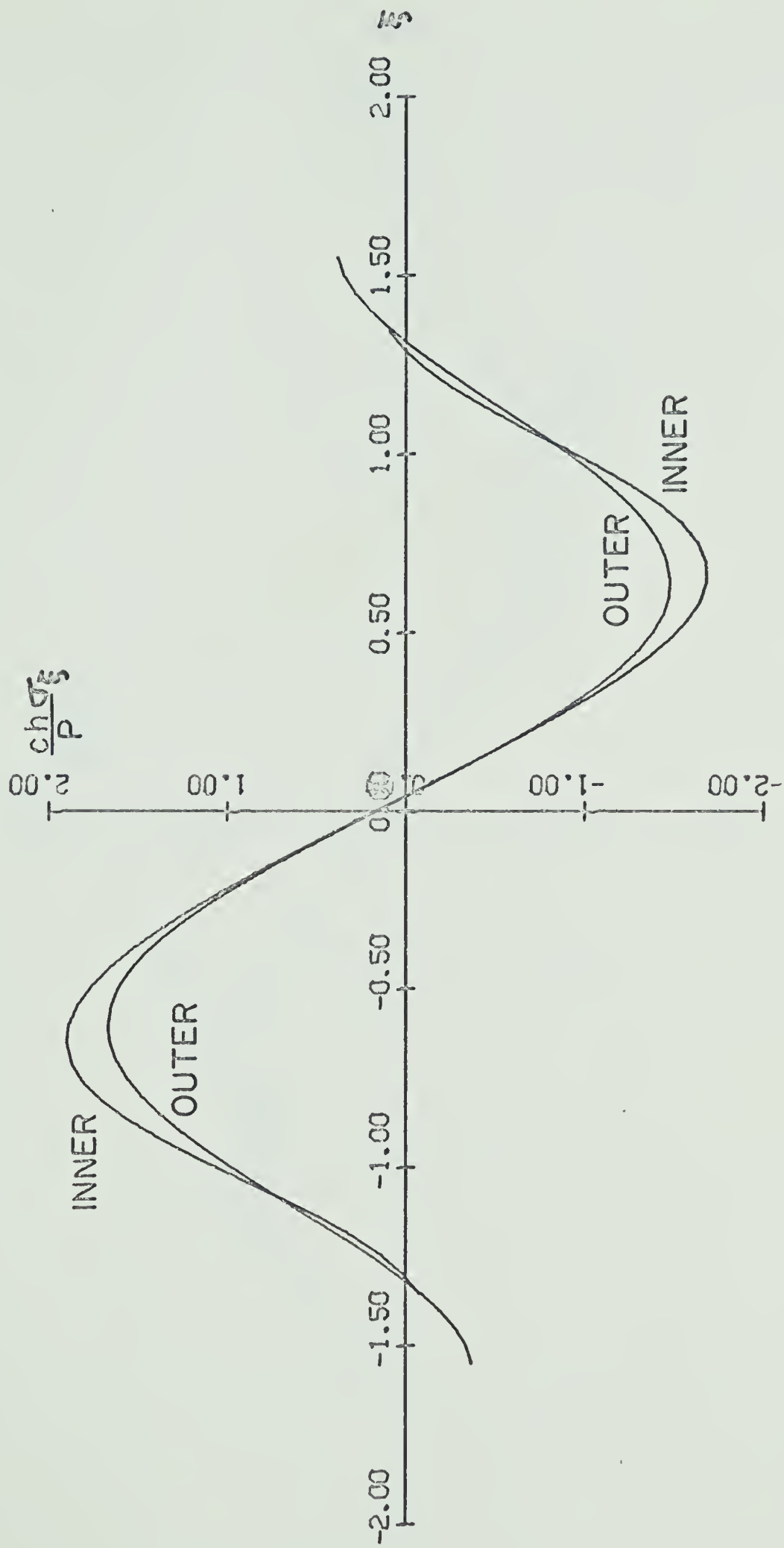


FIGURE 4.1 INNER & OUTER SOLUTIONS (RADIAL)

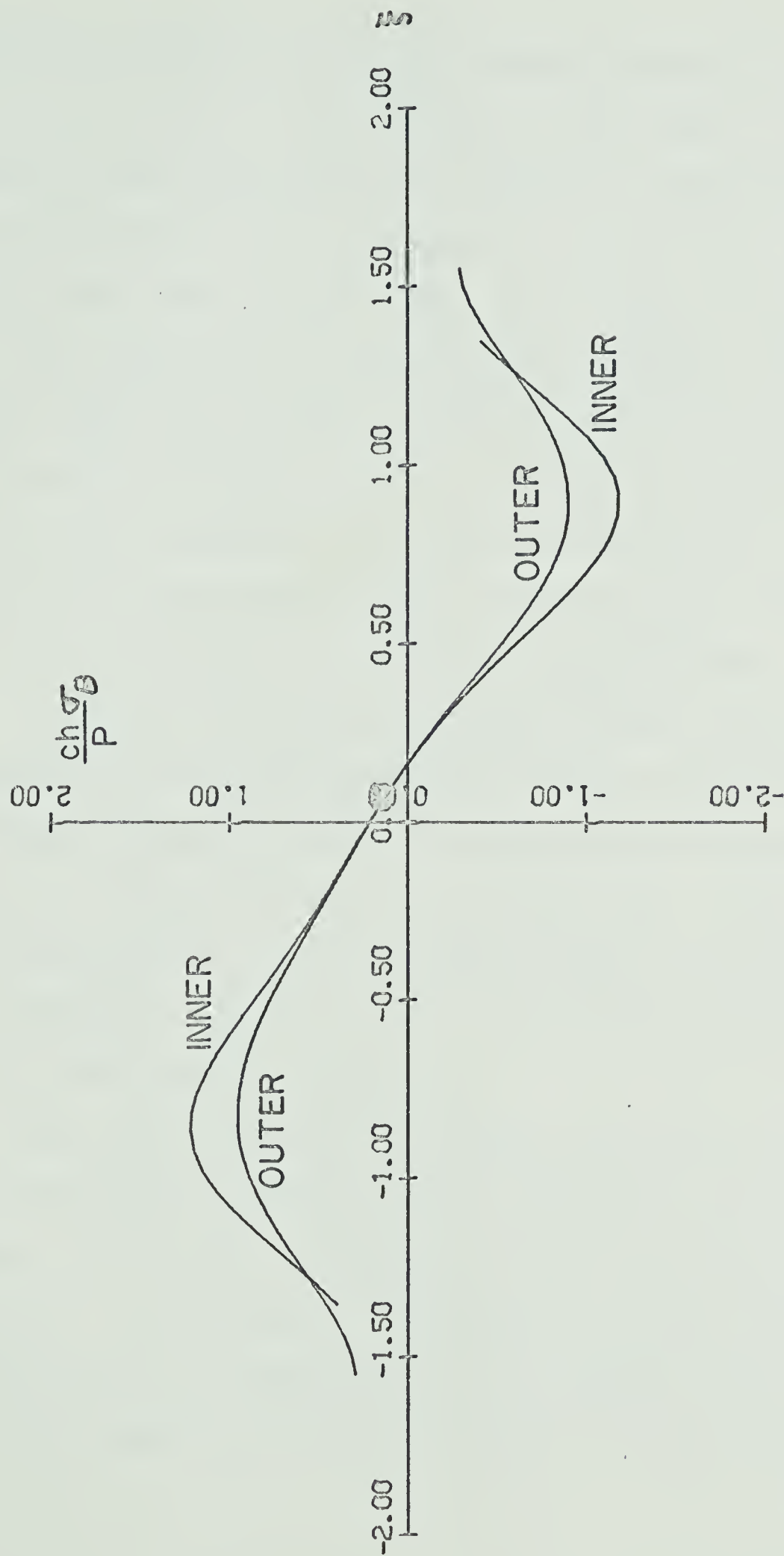


FIGURE 4.2 INNER & OUTER SOLUTIONS (CIRCUMFERENTIAL)

distributions are plotted to show the difference between the theoretical and experimental results. Since the direct radial stress is small as compared to the bending stress, the difference in magnitude between the inside and outside stress is negligible. In the region surrounding the origin, the present solution follows that of Clark's very closely. However, for ξ greater than ± 0.40 the variation becomes very distinct. At $\xi = 0.85$, the present solution predicts a stress of 25% higher than that of Clark's. For larger values of ξ , the two inner solutions converge to the outer solution. The solution presented here is in better agreement with the experimental points than Clark's, thus indicating the validity of the solution in the region of maximum stress.

The inside and outside experimental stresses and the circumferential stress for both theories are plotted in figure 4.4. The difference between the theories is more pronounced throughout the range of ξ than was the case for the radial stress. Again at the point of maximum stress, the present theory predicts a circumferential stress of 25% higher than that by Clark. Both theories converge to the outer solution for large values of ξ .

The stress distributions in figures 4.3 and 4.4 are plotted for the inside surface of a bellow under a compressive axial load. The stresses on the inside surface give a stress distribution similar to the theory. For the outside circumferential stresses, the stress corresponding to N_0 is of opposite sign to the bending stress, yielding a distribution completely different from that of the inside surface.

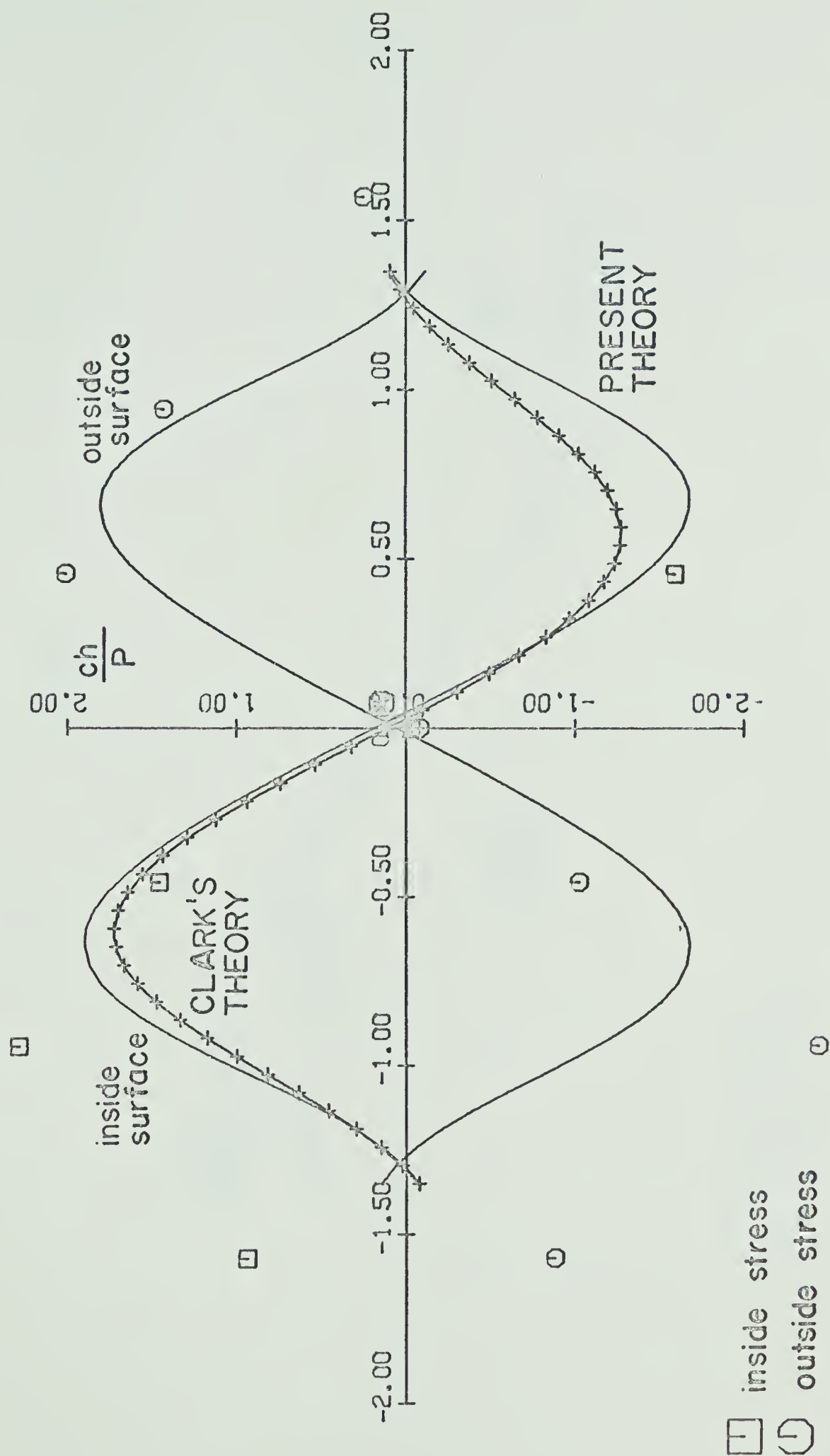


FIGURE 4.3 RADIAL STRESSES
INSIDE SURFACE

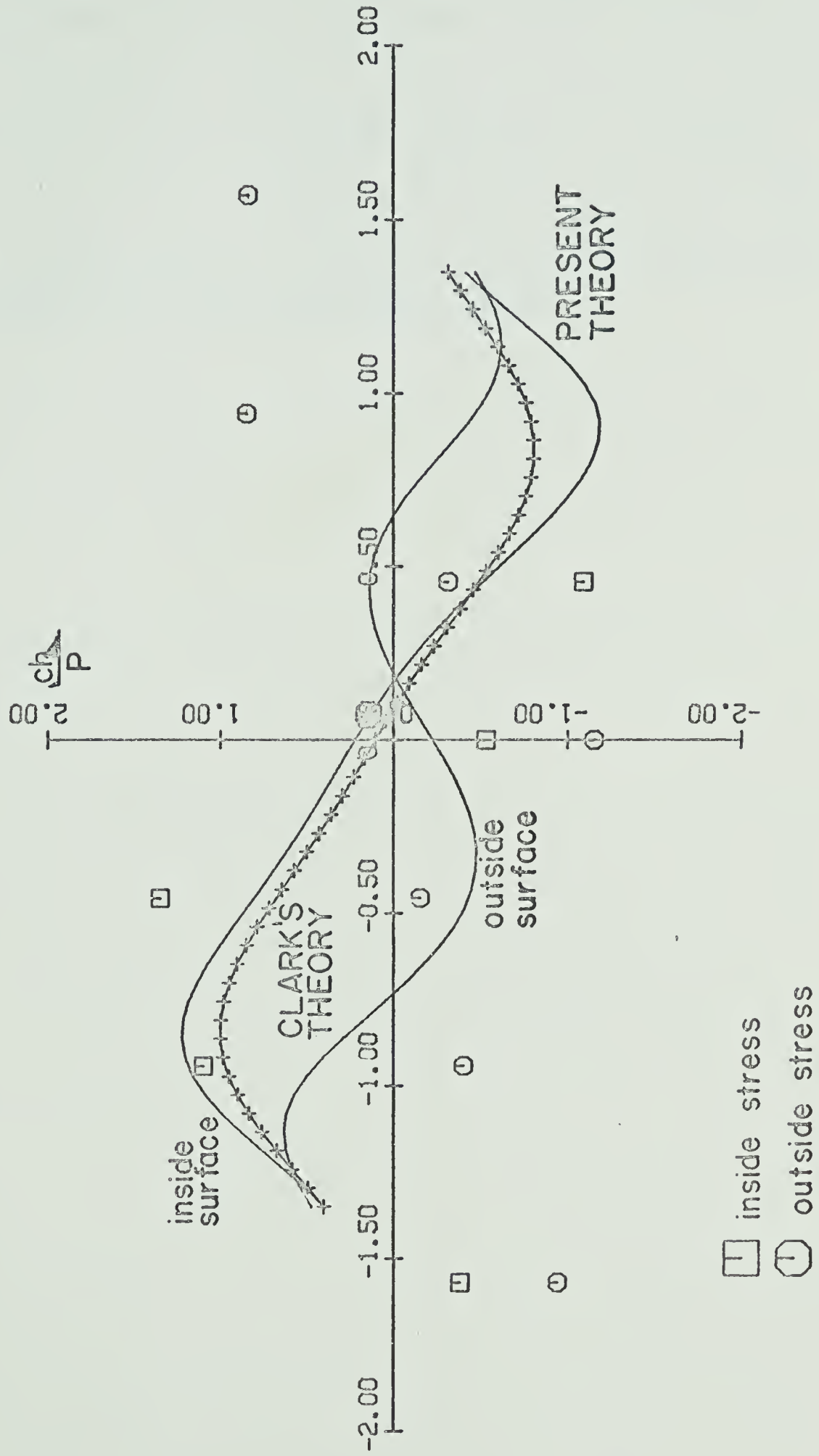


FIGURE 4.4 CIRCUMFERENTIAL STRESSES INSIDE SURFACE

The poor agreement between the experimental and the theoretical values for the circumferential stress on the outer surface can be contributed to the variation of the wall thickness throughout a corrugation.

Another source of error would be due to the difficulty in mounting the strain gauges; however, the present theoretical analysis seems to fit reasonably well to the experimental results.

CHAPTER V

CONCLUDING REMARKS

The major conclusions that can be drawn from the theoretical analysis and experimental investigation are:

(1) The stresses are very sensitive to variations in the wall thickness. An increase of 0.005 inches in h produces an increase in the experimental stress by 15%, while the theoretical stress decreases by 15%.

(2) Because of the high dependence upon h , manufacturers should incorporate in their specifications the minimum wall thickness of the bellow.

(3) The experimental and theoretical values calculated for the stresses do not differ by more than 30%. Since an average value of .035 inches was used for the bellow thickness, and the actual values vary from this figure up to .005 inches, the discrepancy between theoretical and experimental stress values is within the bounds of experimental error.

LIST OF REFERENCES

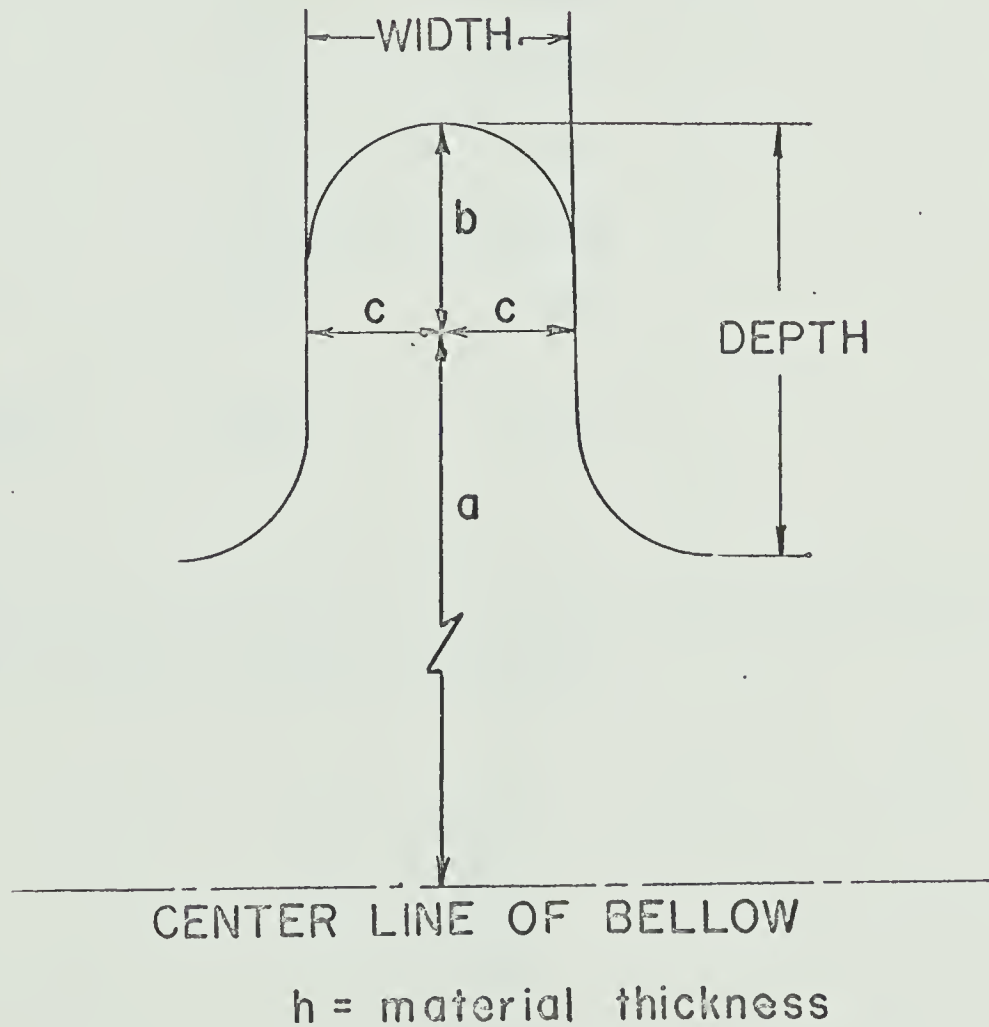
1. Reissner, E., "On Stresses and Deformations in Toroidal Shells of Circular Cross Section which are Acted Upon by Uniform Normal Pressure", Quart. Appl. Math. 21 (1963), pp. 177-187.
2. Clark, R.A., "On the Theory of Thin Elastic Toroidal Shells", Journal of Mathematics and Physics, Vol. 29, 1950, pp. 146-178.
3. Clark, R.A., "An Expansion Bellows Problem", Journal of Applied Mechanics, March, 1970, pp. 61-69.
4. Reissner, E., "On Axisymmetrical Deformations of Thin Shells of Revolution", Proc. Symposia in Appl. Math. 3 (1950), pp. 27-52.
5. Reissner, E., "On the Theory of Thin Elastic Shells", Reissner Anniversary Vol. (1959), pp. 231-247.
6. Laupe, A. and Weil, N.A., "Analysis of U-shaped Expansion Joints", Journal of Applied Mechanics, Vol. 29, Trans. ASME, Vol. 84, Series E, 1962, pp. 115-123.
7. Acton, F.S., "Numerical Methods that Work", Harper & Rowe (1970), pp. 194-195.



APPENDIX A

DETERMINATION OF EXPERIMENTAL PARAMETERS

Average values for the physical parameters a , b , c and h were determined prior to any experimental tests. Vernier calipers were used for all measurements.



Measurements

	<u>Depth (inches)</u>	<u>Width (inches)</u>
	2.157	1.365
	2.182	1.363
	2.165	1.330
	2.130	1.360
	2.177	1.325
	2.168	1.353
	2.165	1.342
	2.190	1.335
	2.192	1.330
	2.160	1.340
	2.127	1.325
Average	2.158	1.341

Using the average values from above, the particular bellow considered here has the following dimensions

$$a = 5.074"$$

$$b = 1.074"$$

$$c = 0.672"$$

$$h = 0.035"$$

APPENDIX B
EXPERIMENTAL DATA

Test #1

Strain Gauge (micro inches per inch)	Load (pounds)			
	100	200	300	400
1				
2	135	330	525	716
3	285	605	902	1185
4	34	102	146	170
5	-108	-270	-420	-552
6	-290	-638	-960	-1260
7	- 45	-142	-250	-350
8	100	210	320	434
9	60	120	172	220
10	-110	-242	-375	-510
11	-145	-306	-458	-600
12	15	42	70	102
13	40	90	145	200
14	- 86	-182	-266	-352
15	- 83	-175	-260	-340
16	50	110	174	244
17	122	248	375	494
18	- 60	-134	-208	-280
19	- 68	-158	-246	-337
20	130	282	433	582
21	256	538	794	1036
22	136	288	426	548
23	- 6	18	62	123
24	-182	-362	-504	-628

Test #2

Strain Gauge (micro inches per inch)	Load (pounds)			
	100	200	300	400
1				
2	166	360	571	733
3	306	630	945	1195
4	54	106	165	155
5	- 95	-275	-402	-572
6	-292	-659	-960	-1290
7	- 93	-150	-235	-380
8	109	220	327	434
9	64	124	175	222
10	-123	-257	-392	-530
11	-163	-325	-477	-624
12	16	46	76	112
13	42	92	148	204
14	-101	-196	-280	-364
15	-100	-194	-277	-357
16	54	118	180	248
17	130	264	386	510
18	- 70	-150	-222	-295
19	- 85	-170	-263	-355
20	148	304	455	606
21	287	572	826	1072
22	158	312	446	570
23	5	28	76	133
24	-201	-375	-516	-637

Test #3

Strain Gauge (micro-inches per inch)	Load (pounds)			
	100	200	300	400
1				
2	153	330	513	706
3	296	600	894	1170
4	33	66	96	120
5	-124	-315	-480	-606
6	-329	-705	-1038	-1340
7	- 56	-190	-309	-414
8	111	222	330	436
9	64	124	174	221
10	-130	-263	-400	-540
11	-170	-332	-486	-633
12	18	46	76	108
13	43	95	148	205
14	-106	-200	-288	-372
15	-104	-198	-280	-363
16	60	121	184	250
17	139	267	392	504
18	- 76	-152	-230	-303
19	- 90	-180	-270	-364
20	154	310	461	614
21	300	582	840	1084
22	164	318	450	574
23	0	32	81	135
24	-206	-382	-524	-642

Test #4

Strain Gauge (micro-inches per inch)	Load (pounds)			
	100	200	300	400
1				
2	131	326	500	687
3	278	594	880	1150
4	12	65	90	101
5	-145	-320	-479	-624
6	-347	-713	-1040	-1355
7	- 70	-190	-306	-429
8	110	222	330	436
9	63	124	174	221
10	-130	-264	-400	-540
11	-170	-333	-485	-633
12	18	46	75	107
13	42	93	148	205
14	-105	-201	-288	-371
15	-106	-200	-284	-362
16	53	120	181	252
17	134	269	388	510
18	- 75	-154	-228	-303
19	- 90	-177	-271	-366
20	152	310	460	612
21	302	584	838	1082
22	162	318	450	572
23	2	38	79	137
24	-206	-382	-524	-644

Average of Tests

Strain Gauges (micro-inches per inch)	Load (pounds)			
	100	200	300	400
1				
2	146	336	527	710
3	291	607	905	1175
4	33	85	124	136
5	-118	-295	-445	-558
6	-314	-679	-999	-1311
7	- 66	-168	-276	-393
8	107	218	327	435
9	63	123	174	221
10	-123	-256	-392	-530
11	-162	-324	-476	-622
12	17	45	74	107
13	42	92	147	203
14	-100	-195	-280	-365
15	- 98	-192	-275	-355
16	54	117	180	248
17	131	262	385	504
18	- 70	-147	-222	-295
19	- 83	-171	-262	-355
20	146	301	452	603
21	286	569	824	1068
22	155	309	443	566
23	0	29	74	132
24	-199	-375	-517	-638

APPENDIX C

VALUES OF $f(\rho)$ AND $g(\rho)$ Calculations of the function f and g

The numerical method used consisted of a Hamming's modified predictor corrector for the integration of equations (2.23) and (2.24). In order to use this procedure, the initial conditions $f(0)$, $f'(0)$, $g(0)$, $g'(0)$ must be specified. We know two conditions since the functions f and g are both even values in ρ . The other initial conditions were found by adapting Newton's method for quadratic polynomial factors [7]. The criterion used for the determination of the correct value was that the functions should be equal to their asymptotic expansion at $\rho = 5.0$. Since only one condition can be satisfied for each function it is impossible to specify that the slopes of the functions should be equal to those of their asymptotic expansions. However, in the region $\rho = 5.0$, the slopes do match within the accuracy specified for the values of the functions.

In figure 2.5 and 2.6, the values of f and g are found by the numerical integration for $\rho < 5.0$, while for $\rho > 5.0$, the asymptotic expansion is used. These values of f , f' , f and g' are similar to the function $T_{2,0}(x)$ which is described in [3]. The relations between these functions are

$$f(\rho) = - \operatorname{Re} T_{2,0}(\rho)$$

$$g(\rho) = \operatorname{Im} T_{2,0}(\rho)$$

$$f'(\rho) = - \operatorname{Re} T_{2,0}'(\rho)$$

$$g'(\rho) = \operatorname{Im} T_{2,0}'(\rho)$$

The values of the functions and their derivatives for $\rho \leq 5.0$ are given below.

ρ	$f(\rho)$	$f'(\rho)$	$g(\rho)$	$g'(\rho)$
0	-0.9270	0.0000	-0.9270	0.0000
0.1	-0.9220	0.0997	-0.9270	0.0003
0.2	-0.9072	0.1975	-0.9269	0.0024
0.3	-0.8827	0.2917	-0.9264	0.0081
0.4	-0.8490	0.3802	-0.9251	0.0188
0.5	-0.8069	0.4615	-0.9225	0.0356
0.6	-0.7570	0.5336	-0.9178	0.0593
0.7	-0.7005	0.5948	-0.9104	0.0901
0.8	-0.6385	0.6439	-0.8995	0.1278
0.9	-0.5722	0.6793	-0.8846	0.1715
1.0	-0.5031	0.7003	-0.8651	0.2199
1.1	-0.4326	0.7062	-0.8405	0.2714
1.2	-0.3624	0.6969	-0.8108	0.3239
1.3	-0.2937	0.6730	-0.7758	0.3750
1.4	-0.2282	0.6351	-0.7359	0.4224
1.5	-0.1671	0.5850	-0.6915	0.4637
1.6	-0.1116	0.5247	-0.6434	0.4969
1.7	-0.0624	0.4566	-0.5925	0.5203
1.8	-0.0204	0.3832	-0.5397	0.5328
1.9	0.0141	0.3077	-0.4863	0.5336
2.0	0.0411	0.2330	-0.4334	0.5226
2.1	0.0609	0.1620	-0.3821	0.5009
2.2	0.0737	0.0969	-0.3335	0.4695
2.3	0.0805	0.0396	-0.2885	0.4302
2.4	0.0820	-0.0081	-0.2477	0.3851
2.5	0.0792	-0.0455	-0.2116	0.3364

ρ	$f(\rho)$	$f'(\rho)$	$g(\rho)$	$g'(\rho)$
2.6	0.0732	-0.0726	-0.1804	0.2869
2.7	0.0650	-0.0898	-0.1542	0.2382
2.8	0.0556	-0.0978	-0.1327	0.1926
2.9	0.0457	-0.0982	-0.1155	0.1516
3.0	0.0361	-0.0927	-0.1022	0.1161
3.1	0.0273	-0.0828	-0.0921	0.0865
3.2	0.0197	-0.0701	-0.0846	0.0634
3.3	0.0133	-0.0566	-0.0792	0.0462
3.4	0.0084	-0.0431	-0.0752	0.0341
3.5	0.0047	-0.0307	-0.0722	0.0266
3.6	0.0021	-0.0203	-0.0698	0.0224
3.7	0.0006	-0.0118	-0.0677	0.0206
3.8	-0.0003	-0.0056	-0.0656	0.0206
3.9	-0.0006	-0.0013	-0.0635	0.0212
4.0	-0.0006	0.0014	-0.0614	0.0223
4.1	-0.0004	0.0024	-0.0591	0.0232
4.2	-0.0001	0.0028	-0.0567	0.0236
4.3	0.0001	0.0024	-0.0544	0.0237
4.4	0.0003	0.0018	-0.0520	0.0232
4.5	0.0005	0.0011	-0.0497	0.0224
4.6	0.0006	0.0004	-0.0476	0.0213
4.7	0.0006	-0.0001	-0.0454	0.0201
4.8	0.0005	-0.0005	-0.0435	0.0188
4.9	0.0003	-0.0008	-0.0417	0.0177
5.0	0.0004	-0.0008	-0.0400	0.0166

B29993